Commissioning and Characterization of Charge Conversion Particle Sources

Master's Thesis in Physics

Presented by
Maximilian Wecker
June 3, 2024

Friedrich-Alexander-Universität Erlangen-Nürnberg

Supervisors: Dr. Martin Wieser and Prof. Dr. Jörn Wilms

Carried out at the Swedish Institute of Space Physics

Abstract

The Sun continuously produces solar wind, which is fully ionized plasma that flows radially away from the Sun. When the charged particles of the solar wind interact with the surface of the Moon, scattering and sputtering occur. Both processes are expected to produce neutral atoms, positive ions, and negative ions. Unlike for the former two particle species, the observation of negative ions has never been reported. The space instrument Negative Ions at the Lunar Surface (NILS) was developed at the Swedish Institute of Space Physics (IRF) to change that. NILS is one of the international payloads onboard the Chinese Chang'E-6 mission to the moon. The goal of Chang'E-6 is to land on the far side and return lunar surface samples. NILS is mounted on the lander and its aim is the search for and characterization of negatively charged ions at the lunar surface. One step in the development of NILS is the calibration of the instrument for which a negative ion beam is necessary. The duoplasmatron particle source in the calibration facility at IRF can only provide positive ions. Therefore a charge conversion particle source was used to convert the positive ion beam into a negative one.

In my thesis work I experimentally characterized the charge conversion particle source, which has previously been used to provide negative ions for the calibration campaign of NILS. The source is called Negative IOn Source (NIOS). It converts the positive ions from the primary beam into negative ions by charge conversion upon scattering at grazing incidence from an aluminium surface. I characterized NIOS by conducting spatial scans with a Faraday cup. I measured seven current density profiles for seven different primary beam energies between 450 eV and 5000 eV. The experimental characterization was done in the calibration system for particle instruments at IRF, the same facility where NILS was calibrated. I handed over the data and they were used to calibrate NILS.

I also performed simulations of NIOS using the ion-optical software package SIMION, which were validated and improved using the experimental results. Additionally to the basic features offered by SIMION, I manually implemented particle scattering at the scattering surface, charge conversion, molecule dissociation, secondary electron emission, and Earth's magnetic field. The simulation was not able to explain an electron population measured by NILS. The most likely cause is the lack of multiple scattering. The ions and neutrals were simulated satisfyingly, which was the primary goal. The simulation was the foundation for the subsequent optimization.

During the characterization and simulation I identified multiple problems, e.g., a portion of the primary beam that can travel through NIOS without any surface interaction. I optimized the geometry using an implementation of a genetic algorithm. The new model of NIOS does not show the identified problems anymore. The new model features an ion yield increase by a factor of 2.7 from 0.47 % for the old model to 1.27 %. The new model has been manufactured in the workshop at IRF and is going to be used for future instrument calibration campaigns.

Kurzzusammenfassung

Neben Photonen stößt die Sonne auch kontinuierlich vollionisiertes Plasma aus, den sogenannten Sonnenwind. Das Plasma bewegt sich radial von der Sonne weg. Die geladenen Teilchen des Sonnenwindes können mit der Mondoberfläche interagieren, indem sie unter anderem sputtern und streuen. Es wurde vorhergesagt, dass diese beiden Prozesse neutrale Atome, positive Ionen und negative Ionen erzeugen. Die beiden erstgenannten Produkte konnten bereits experimentell nachgewiesen werden. Negative Ionen wurden jedoch bisher nie beobachtet. Das Teilcheninstrument Negative Ions at the Lunar Surface (NILS) wurde am schwedischen Institut für Weltraumphysik (IRF) entwickelt, um dieses Problem zu lösen. Es ist eines der internationalen Instrumente, das im Rahmen der chinesischen Chang'E-6 Mission zum Mond fliegt. NILS befindet sich auf dem Landemodul mit dem es auf der Mondrückseite landet und sein Ziel ist es, dort negative Ionen zu messen. Ein Schritt in der Entwicklung von NILS ist seine Kalibrierung, für die ein negativer Teilchenstrahl benötigt wird. Die Duoplasmatron-Teilchenquelle am IRF kann nur einen positiven Teilchenstrahl erzeugen. Darum wurde eine Teilchenquelle benutzt, die mithilfe von Ladungsumwandlung den positiven Strahl in einen negativen umwandelt.

In meiner Arbeit führte ich die experimentelle Charakterisierung der Umwandlungsquelle durch, die negative Ionen für die Kalibrierung von NILS lieferte. Die Quelle wird Negative IOn Source (NIOS) genannt. In NIOS befindet sich eine Aluminiumfläche, auf der die positiven Ionen unter einem flachen Winkel auftreffen und streuen. Durch diesen Streuprozess entstehen negative Ionen. Die Charakterisierung von NIOS führte ich mit einem Faraday-Becher durch und erlangte Stromdichteprofile für sieben verschiedenen Primärstrahlenergien zwischen 450 eV und 5000 eV. Die Charakterisierung der Quelle wurde in dem selben Kalibrierungssystem durchgeführt, wie auch die Kalibrierung von NILS. Die Daten wurden übergeben und für die Kalibrierung von NILS benutzt.

Mithilfe des ionenoptischen Softwarepakets SIMION, simulierte ich NIOS. Die Simulation wurde durch die Ergebnisse der Charakterisierung validiert und verbessert. Zusätzlich zu den Standardfunktionen von SIMION, implementierte ich Teilchenstreuung an der Streufläche, Ladungsumwandlung, Moleküldissoziation, Sekundärelektronemission und das Magnetfeld der Erde. Die Simulation war nicht in der Lage eine Elektronenpopulation zu erklären, die von NILS gemessen wurde. Die wahrscheinlichste Ursache dafür ist das Fehlen von Mehrfachstreuung. Die Simulation von Ionen und neutralen Atomen – das Hauptziel – war hingegen zufriedenstellend. Die erfolgreiche Simulation bildete das Fundament für die folgende Optimierung.

Während der Charakterisierung und Simulation identifizierte ich mehrere Probleme, z. B. die Tatsache, dass ein Teil der Primärionen ohne Oberflächeninteraktion durch NIOS durch fliegen kann. Ich optimierte die Geometrie von NIOS mithilfe einer Implementierung eines genetischen Algorithmus. Das neue Modell von NIOS weist die Probleme nicht mehr auf. Der Ertrag von negativen Ionen wurde um den Faktor 2.7 verbessert, von 0.47 % auf 1.27 %. Das neue Modell wurde bereits in der Werkstatt des IRF gefertigt. Es wird für die Kalibrierung zukünftiger Instrumente benutzt werden.

Contents

1 Introduction

1.1 Scientific Background and Motivation

The surfaces of airless bodies in the solar system (moons, asteroids, meteoroids) are constantly subject to particle bombardment by the solar wind. The solar wind is a fully ionized plasma mainly consisting of protons (H^+), alpha particles (He^{++}) and low densities of highly ionized heavy ions (e.g., carbon (C), nitrogen (N), oxygen (O), etc.) flowing away radially from the sun (Borovsky, 2020). Because of the lack of a protective atmosphere and magnetic field, the particles of the solar wind can reach the surface of these bodies. However, even bodies that have no inherent magnetosphere can have local magnetic anomalies that shield them partially from incoming charged particles (Lue et al., 2011). Depending on the particular body, the particles that reach the surface will often meet regolith there. Regolith is the mantling loose material of bodies that covers consolidated bedrock (Scott and Pain, 2009). It exists on various bodies, such as the Moon and Earth, and is created by (depending on the present processes) weathering, erosion, and transport and/or deposition of older material (Scott and Pain, 2009). Especially for the relatively unprotected Moon, the exposure to different kinds of precipitation from space forms the regolith (e.g. impacts from micrometeoroids, solar photons, solar wind particles, cosmic ray particles, etc.) (Wieser et al., 2020). This leads to the question: How do the surfaces of airless, unprotected bodies change over time due to the solar wind?

In the past, the lunar regolith was thought to absorb 99 % of the protons coming from the solar wind (Crider and Vondrak, 2002). However, recent missions (Kaguya (Saito et al., 2008), Chang'E-1 (Ouyang et al., 2010), Chandrayaan-1 (Barabash et al., 2009), ARTEMIS (Angelopoulos, 2011) and IBEX (McComas et al., 2009a)) have shown that a variety of unexpected processes lead to a zoo of particles emitted from the surface (Wieser et al., 2020). The emitted particles – such as sputtered atoms (Hoffman and Hodges, 1975), scattered ions (Holmström et al., 2010) and neutrals (McComas et al., 2009b), and secondary electrons (Willis et al., 1973) – feed the lunar exosphere. That is the region of any atmosphere, where the mean free path of particles (distance between two collisions) is larger than the scale height (altitude at which the atmospheric density decreased to a factor of $1/e$). On Earth this altitude is at about 500 km (Grava and Retherford, 2023). On the Moon the condition is met at the surface, effectively creating a surface-bound exosphere (Grava and Retherford, 2023). The different animals in the aforementioned zoo of emitted particles are of great interest, because the interactions creating them are possible sources for the production of hydroxyl groups and water in the regolith on the moon (Pieters et al., 2009). In order to gain knowledge about the

interactions, we have to study their products.

But why is that important? Why should we care about these solar wind-surface interactions? Two overarching aspects come to mind: First, sources for hydroxyl groups and water are of great interest. We are at the start of a new space exploration era. Several governmental and private organizations have recently (re-)gained interest in going to the Moon (see, e.g., NASA's Artemis campaign (Smith et al., 2020)) as an intermediate step to eventually sending humans to Mars. Naturally, minimizing the costs of sustaining an extraterrestrial outpost is critical. This can be achieved by making use of in-situ resources. Hydroxyl groups and water can potentially be turned into fuel for regenerative fuel cells using oxygen and hydrogen (National Research Council, 2007). Since the solar wind-surface interaction is one of the possible origins of these resources, it is important to understand the underlying process in detail.

The second overarching aspect takes into account that the Moon is a natural laboratory for regolith and exosphere processes on airless bodies that is accessible to humans (National Research Council, 2007). Knowledge gained on the Moon often is applicable to other bodies, which are much harder to reach. That way we can learn about the evolution of a whole category of bodies. The committee on "The Scientific Context for Exploration of the Moon" (National Research Council, 2007) warns, however, to determine the global density, composition, and time variability of the fragile lunar atmosphere before it is perturbed by further human activity.

On the way to gain a full picture of solar wind-surface interactions, positive ions were observed (e.g., Saito et al. (2008)) as well as energetic neutral atoms (e.g., Wieser et al. (2024)). What is missing is the negative ion population. Wekhof (1981) predicted that charge inversion during energetic proton scattering on the lunar surface leads to negative ion emission. However, no observation of negative ions has been reported yet (Xin, 2024), even though there were missions, which in principle were capable of detecting them, e.g., Kaguya with its electron spectrum analyzer (Saito et al., 2008). When the solar wind interacts with the lunar surface, there are two categories of products: particles that stay on the surface and particles that leave it. Investigating the former is comparatively hard and entails sample return missions to earth. Investigating the other type is "easier" due to remote sensing. This can be achieved either via a probe in orbit or through in-situ observations conducted by a lunar lander. A lander allows for measurements with a distance to the surface in the range of meters, compared to about 100 km for orbiters. Reasons for the apparent absence of negative ions at orbit distance can be that either they are simply very rare or they are neutralized too quickly. According to Wekhof (1981), photodetachment (i.e., a photon transfers energy to a bound electron such that the electron is detached from the atom, $H^- + \gamma \rightarrow H + e^-$) limits the lifetime of H^- to about 0.5 s. That corresponds to an altitude of about 100 km that the negative ions can reach, before they are neutralized. Potentially, they simply cannot be detected by orbiters because of that. The solution to this problem is a negative ion instrument at the lunar surface. The overarching science question, formulated in Wieser (2019), is:

> "How important are negative ions for space-surface interactions and environments of planetary surface-bound exospheres?"

Figure 1.1: Assembly of Chang'E-6 spacecraft. On the left side, from top to bottom, there is the ascender, the lander and the returner. On the right side there is the orbiter. The NILS instrument (red circle) is mounted on the lander. Image credit: CNSA/CLEP.

1.2 Chang'E-6

1.2.1 Mission Overview

On 3rd of May 2024 the China National Space Administration (CNSA) launched the Chang'E-6 (Xin, 2024) mission to the Moon. Chang'E-6 is a sample return mission. Like its predecessor Chang'E-5, Chang'E-6 will collect mineral samples and send them back to Earth. The landing site is in the South Pole-Aitken (SPA) basin on the lunar far side. The location makes the mission particularly challenging, but also particularly interesting. The basin is the largest and oldest impact crater on the Moon. Samples from this region can help answering questions about the early history of the Moon.

The spacecraft (Figure 1.1) consists of four components, an orbiter, a lander, an ascender, and a re-entry module called returner. Xin (2024) describes the scheme of the mission. When the spacecraft reaches the Moon, it separates into two parts. The orbiter and the returner remain in orbit and the lander and ascender land on the lunar surface. Since the lunar far side is not visible from Earth, a relay satellite is necessary to be able to communicate with the lander of Chang'E-6. The relay satellite is called Queqiao-2 and has been sent to a highly elliptical orbit around the Moon, one month prior to the

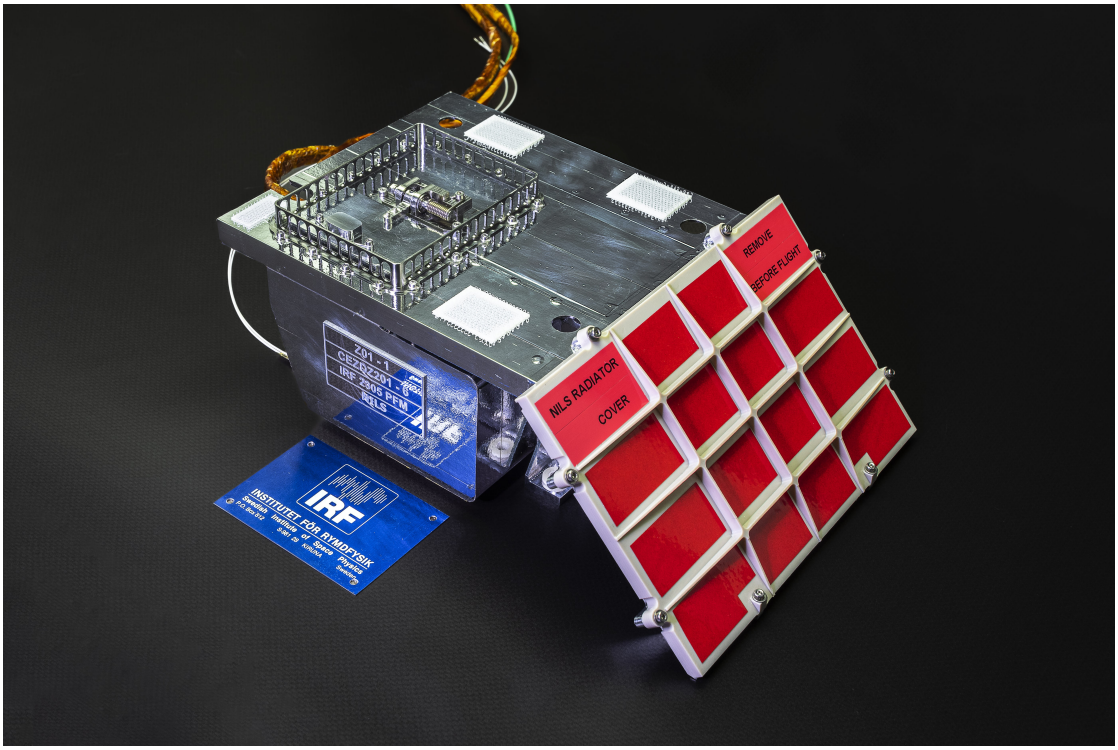

Figure 1.2: Close-up of Negative Ions at the Lunar Surface instrument. The (closed) aperture is located in the center, within the area surrounded by a fence-like structure. The angled surface, covered by a red protection surface, is a thermal radiator. Image Credit: Romain Canu-Blot, personal communication.

launch of Chang'E-6. When the collection of the samples is completed, the ascender returns to the orbiter in space, while the lander stays on the surface. The ascender docks to the orbiter/returner, hands over the samples, undocks, and crashes into the Moon. The orbiter/returner then head home to Earth. Upon their arrival, they separate and the returner is planned to land in China.

Chang'E-6 carries several international payloads: Pakistan's first lunar satellite ICUBE-Q, the Italian INstrument for landing-Roving laser Retroreflector Investigations (INRRI), the French instrument for Detection of Outgassing RadoN (DORN), and the Swedish Negative Ions at the Lunar Surface (NILS) instrument.

1.2.2 The NILS payload

On behalf of the European Space Agency (ESA), the Swedish Institute of Space Physics (IRF) participates in the Chang'E-6 mission by providing a negative ion instrument, NILS (Figure 1.2). It is dedicated to answer the aforementioned scientific question, which translates to the following more detailed science objectives (from Wieser, 2019):

Table 1.1: NILS performance. Credit: Romain Canu-Blot, personal communication.

Parameter	Value
Energy range E/q	10 eV/q - 3 keV/q
Field of view	120° × 15°
Angular resolution	15° × 7° (FWHM)
Mass resolution	m/q groups: 1, 4, 16, ≥ 28
Energy resolution	12 %
Geometric factor	1.3×10^{-4} cm^2 sr eV/ eV
Time resolution	4.0 s to 6.2 s (one direction)
	105 s (full coverage)
Power consumption	≈ 2.3 W
Mass	915 g without MLI

- "How large is the fraction of negative ions in scattering and sputtering from lunar regolith?"
- "How do the negative charge fractions depend on the energy and species of the scattered/sputtered particles?"
- "Do negative ions significantly contribute to and affect the lunar plasma environment?"
- "Do negative ions constitute a substantial loss path for lunar surface elements?"

The performance of NILS is listed in Table 1.1.

NILS is mounted on the Chang'E-6 lander (see red circle in Figure 1.1). For thermal reasons NILS is covered with black multi-layer insulation. When the lander reaches its destination, NILS is at a height of about 2 m above the ground, pointing in front of the lander, towards the surface. It operates for a duration in the range of hours, hopefully leading to data that help answering the scientific questions above.

1.2.3 Calibration of NILS

A crucial step in the development of NILS is its calibration. We can phrase the task as answering the question: "What does NILS report, when exposed to a negative ion beam of known intensity?". Once the calibration is completed, we are able to answer the question in the other direction. We can measure an unknown input and because we know what NILS reports for certain inputs, we can infer the characteristics of the source.

For the calibration we need a negative ion source. The particle source at IRF provides positive ions in its default configuration. In principle, there is a way to create negative ions, but that requires complete rewiring of the source, so it is not done. A charge conversion particle source is used instead, which transforms a portion of the positive ion beam into a negative one. The ion charge state is changed by scattering the initially positive ions at a grazing incidence from an aluminium surface. The first task of this thesis is to characterize the charge conversion particle source used to calibrate NILS. Furthermore,

we will use an ion optical software package to simulate the charge conversion particle source, and optimize its geometry such that an improved version can be manufactured.

2 Characterization

The already available Negative IOn Source (NIOS) was used during the calibration campaign of the NILS instrument to provide negative ions. The negative ion beam profile, the output of NIOS, needs to be characterized. We do this by measuring the electrical current density across the beam profile using a Faraday cup. The characterization is also used to adjust the simulation model of NIOS, which is in turn used to optimize the geometry of an improved NIOS model. In the following sections the available NIOS and its working principle are described. It is described how NIOS is experimentally characterized and the results are presented and discussed.

2.1 Description of NIOS

2.1.1 General Working Principle

The general schematic of NIOS is shown in Figure 2.1. The working principle consists of three steps:
(1) Positive ions enter NIOS coming from the right side. The entrance aperture collimates the ions onto the scattering surface. The white arrow represents the beamline.
(2) the positive ions hit the scattering surface at grazing incidence upon which a large portion gets neutralized. A small portion remains positively charged, another small portion leaves the scattering area negatively charged (Bhattacharya et al., 1980). The exact charge distribution dependents on various parameters, such as energy, scattering angle, beam species, target species, etc. (Verbeek et al., 1980).
(3) The desired negative ion fraction is selected and neutrals and positive ions are rejected by the geometry of NIOS and by the electric field created by electrodes inside of NIOS. The electrodes are set to a negative potential relative to the NIOS body potential. This leads to the formation of an electric field inside NIOS. This field deflects positive ions such that they cannot leave the body and negative ions are guided to the exit aperture. Since the electric field leaves the trajectory of neutrals unchanged, the only way to filter them out is with geometric constrains, e. g. the exact position and dimension of the exit aperture.

2.1.2 Scattering and Charge Exchange on Surfaces

The interaction of particles with surfaces depends on the energy regime and particle species involved. Here we will focus on the conditions present during the experimental part of this work. We investigate low energy (∼0.4–5 keV) hydrogen ions scattering off of an aluminium surface at grazing incidence. The surface interaction is divided into

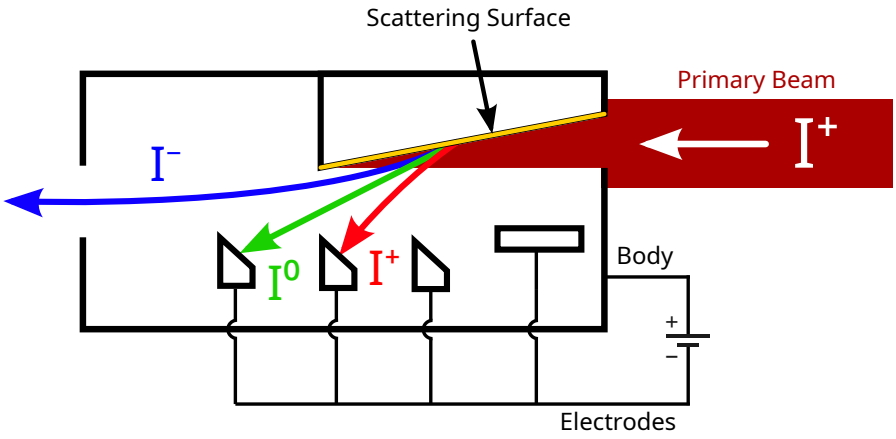

Figure 2.1: Schematic drawing of NIOS. The positive ion beam enters from the right, hits the scattering surface and the three possible particle populations are depicted. The NIOS body is grounded, while the four electrodes are on a negative potential creating an electric field. The field and the geometry filter the particles such that ideally only negative ions are able to leave NIOS through the exit aperture on the left.

two parts: elastic scattering described by a classical trajectory and charge exchange (Heiland, 1994). Ion surface scattering in the energy range of 0.1 keV to 10 keV, can be described by sequences of elastic two-body scattering events (Niehus et al., 1993). We can understand the process as an interaction of two quasi-free particles, because the energy transfer of the ions to the target atom is relatively large compared to the binding energy of the lattice (Niehus et al., 1993). When neutral or ionized H scatters from a surface, the scattered particle can be in one of three possible charge states, H^0, H^+, and H^-. Now the question may arise whether the initial charge state of the incident particle matters. To get to the answer, we need to compare the interaction time with the electron transition time. In other words, do electrons have enough time to transition from or to an incoming ion such that the ion is effectively neutralized before it leaves the interaction region? Summarizing what Heiland (1994) and Niehus et al. (1993) state, the initial charge state of the particle does not influence the final charge state. For steeper impact angles even low energy H penetrates the solid such that the interaction is long enough for neutralization and for flatter impact angles the projectiles stay close to the surface for long enough which leads to the same result.

2.1.3 The Original NIOS

The already available NIOS was designed by modeling the geometry with the help of SIMION (see Dahl, 2000) and implementing simple physical behavior. SIMION is a software package to simulate trajectories of charged particles influenced by electric and magnetic fields. Particles of all three possible charge states were placed uniformly along the scattering surface with a uniform energy distribution ranging from 600 eV to 1000 eV.

The direction followed a uniform distribution inside a 15° half-angle cone along the specular reflection angle. The geometry was then optimized by mainly maximizing the amount of negative particles being able to leave NIOS and minimizing the amount of neutrals and positive particles leaving NIOS.

A technical drawing of NIOS and a 3D-view are depicted in Figure 2.2. NIOS is manufactured out of aluminium and has a length of 151 mm (along the beamline), a width of 160 mm (across the beamline) and a height of 61.1 mm. Looking at the lower left cross section in Figure 2.2, the beamline is defined as a line parallel to the NIOS body, entering NIOS from the left, centered on the entrance aperture. The scattering surface has an inclination of 9.5° relative to the beamline. The beamline therefore hits the scattering surface under the same angle. This leads to particles hitting the surface at grazing incidence. The surface is covered with vapor deposited aluminium tape, which is highly reflective and well suited for scattering. Four electrodes with different shapes (see Figure 2.2) create the electric field which is used to filter the particles. All electrodes have the same potential.

As this NIOS was used for the calibration measurements of NILS, we need to experimentally characterize the output of NIOS.

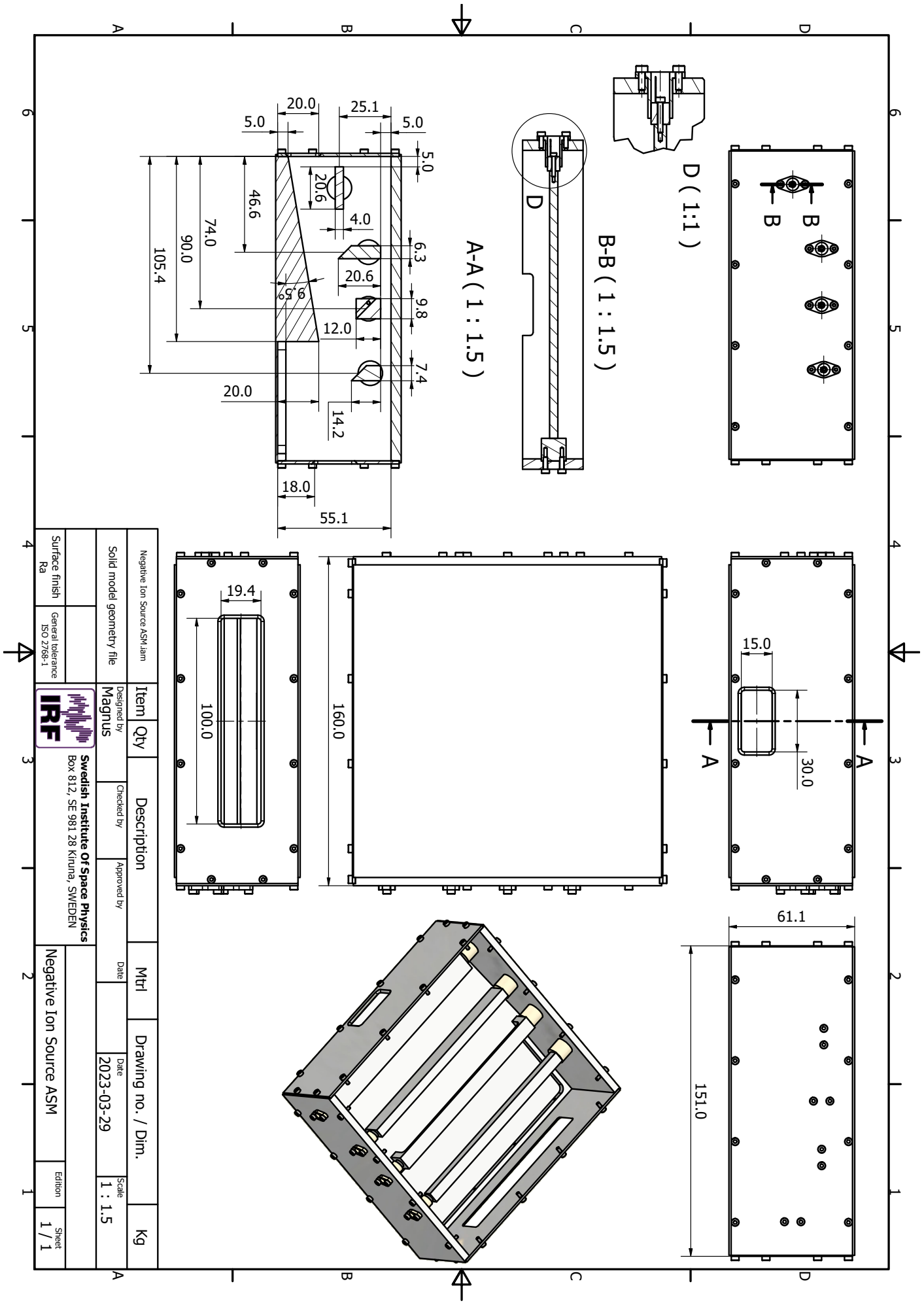

Figure 2.2: Technical drawing of NIOS, provided by IRF.

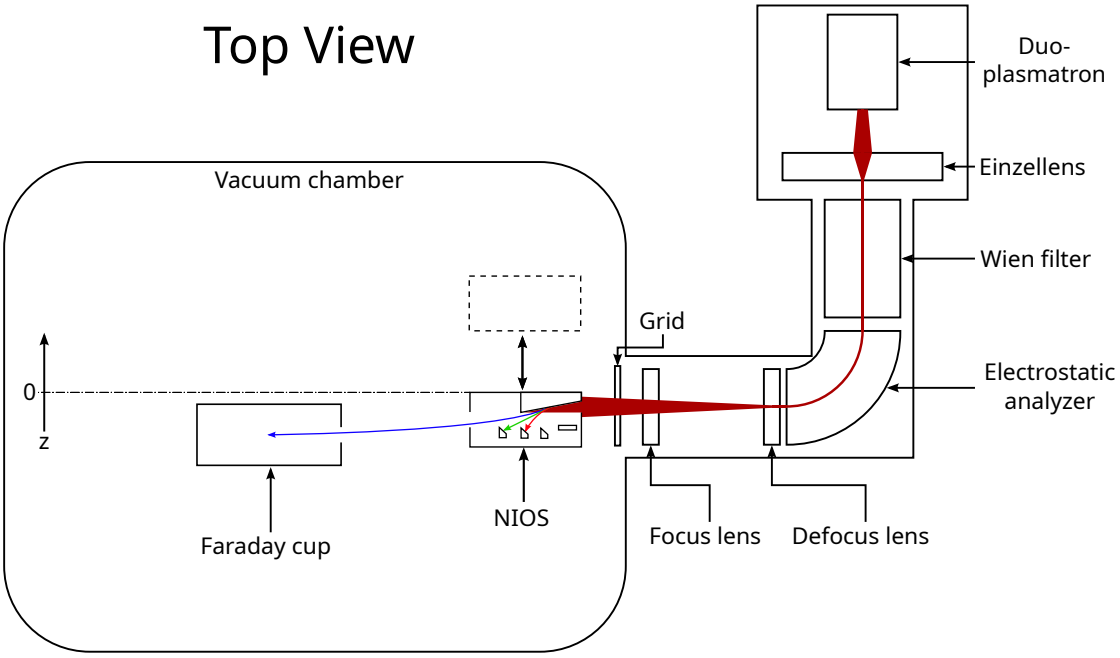

Figure 2.3: Schematic top view of experimental setup for taking spatial scans of beam profile. The beamline is manipulated by various ion optical elements. The grid constantly measures about 10 % of the beam current. The Faraday cup in the center can be moved along the z-axis. The maximum translation range is from -130 mm to 130 mm. The dark-red positive ion beam hits the scattering surface where three possible particle populations are created: light-red for positive ions, green for neutrals and blue for negative ions. Figure modified from Wittmann (2022, p. 135).

2.2 Experimental Setup

NIOS was characterized in the calibration system for particle instruments in IRF's Spacelab. An early version of this system is described in Wuest et al. (2007). The description of the setup follows in parts Wittmann (2022), since the positive ion source used for this work is the same. The setup consists of two main components, the main vacuum chamber with a diameter of 1.2 m and the beam source, which is located outside of the main chamber. The volume, in which the source sits, is connected to the main chamber and is evacuated as well. NIOS and the measurement device, a Faraday cup, are positioned in the main chamber in a vacuum with a pressure of less than 1×10^{-6} mbar. The Faraday cup is a conductive metal cup that collects incoming charged particles. This charges up the cup. If the Faraday cup is connected to an Ampere meter, the cup can discharge, leading to a current measured by the Ampere meter. More details are given in subsection 2.2.2. We use the Faraday cup as our main measuring instrument. A schematic top view of the whole experimental setup is shown in Figure 2.3.

2.2.1 Beam Source

For ion production we use a duoplasmatron source (Carter, 1968). A platinum filament mesh cathode coated with strontium and barium is heated to several hundred degrees Celsius by an electrical current. This leads to thermal electron emission. The electrons are used to strike a discharge arc between the cathode and a pin anode. The arc ionizes the surrounding gas and, depending on the gas composition, different ion species can be extracted. The main ion species we use for characterizing NIOS is H_2^+, yet the source is capable of providing a multitude of species such as H^+, N^+, N_2^+, O^+, O_2^+ and H_2O^+.

The ionization region of the source is set to a positive floating potential with respect to ground, which accelerates the extracted positive ions and gives them their particular kinetic energy. Acceleration voltages for the characterization of NIOS range between 450 eV and 5000 eV. When ions exit the source, they pass through an Einzel lens which focuses the trajectories to a nearly parallel, pencil-like ion beam.

A Wien filter, also called "E-cross-B" or ExB-filter, is then used to select the ion mass per charge. A fixed magnetic field ("B") from a permanent magnet and a variable electric field ("E") are oriented perpendicular to each other. The voltage used to set the variable electric field is denoted "ExB-filter voltage". Both fields lead to forces acting on the charged particles moving through the filter such that only particles with the desired mass per charge can pass through. For a given energy and the selected mass per charge, the Lorentz force (Equation 3.13) is zero, meaning there is no net force acting on the particles, except for gravity, which can be neglected. They travel in a straight line. Particles that do not have the desired charge per particle are subject to a net Lorentz force which deflects them. They cannot travel through the filter.

It is important that the particles have sufficient energy when reaching the ExB-filter. If that is not the case, the beam is not sufficiently parallel and a lot of particles are lost to the walls. Because of that the ion source has two configurations, one for high beam energy (> 1300 eV) and one for low beam energy (< 1300 eV). Since we use beam energies that lie in both regions, both source configurations are used. 1300 eV can be used in either configuration. The low energy mode introduces an additional bias voltage to the ExB-filter that increases the extraction rate of particles from the system. The potential along the first section of the beamline is qualitatively shown in Figure 2.4. For high energies, the ion extraction rate is sufficiently large, because the difference between the floating potential of the ionization region and ground is big enough (see V_{high} in the figure). For low energies the difference to ground, and thus the extraction rate of the system, including the ExB-filter, is too small (see V_{low}). The additional bias in the low energy mode increases the potential difference such that the extraction rate increases. The ions have excess kinetic energy, but because the bias is negative in regards to ground, the particles get decelerated again until they reach ground potential. This results in a sufficiently high amount of particles with the desired, low kinetic energy.

In order to filter out X-rays and neutral particles, an electrostatic analyzer (ESA) bends the ion trajectory by 90°. The electric field inside the ESA creates a force acting on the charged particles. Electron trajectories are bend away from the main vacuum chamber. Neutrals and X-rays are unaffected by the electric field and stay on a straight

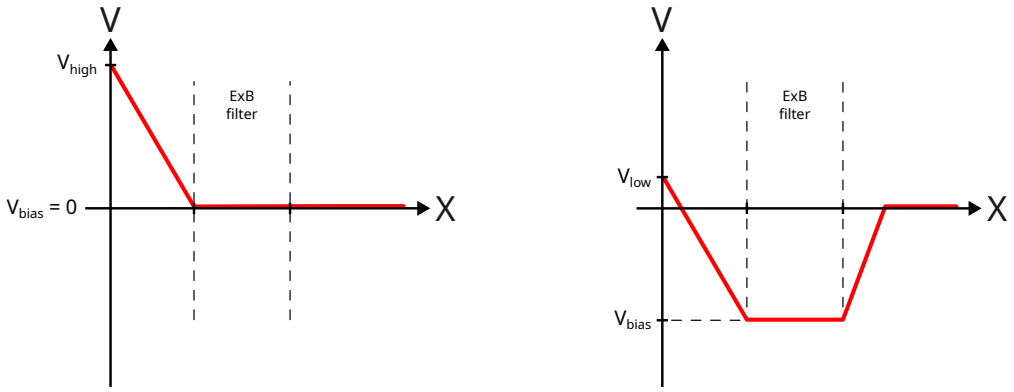

Figure 2.4: Qualitative electric potential along beam line starting from the discharge arc region ($x = 0$). *Left:* For beam energies $> 1300\,\text{eV}$ no additional bias potential is applied. *Right:* For lower energies a negative ExB-filter bias potential is used.

trajectory, hitting the wall. Positive ions are bend towards the main vacuum chamber.

Before entering the main vacuum chamber, the beam can be widened by a defocus lens and re-parallelized by a focus lens which gives it a larger cross-section. That is important, because ideally the entrance aperture of NIOS is fully illuminated by the beam. In practice the beam was only widened, because the effect of the focus lens is very hard to quantify.

2.2.2 Characterizing the Beam

Monitoring the Beam with a Grid

The beam is constantly monitored by a 90 % transparent grid, which is located after the focus lens (see Figure 2.3). Most of the positive ions pass through the grid unaffected. A small fraction is caught by the grid, leading to a grid current I_{grid}, which is used during data analysis to compensate for fluctuations in the beam intensity over time. When ions hit the grid they produce secondary electrons. Since the grid is on the same potential as the surrounding structure, the electrons can easily escape. As a result, the measured total grid current is higher than the positive ion current hitting the grid. This is not a problem, because the grid current only plays a role as a relative ratio of two grid currents in the data analysis.

Measuring with Faraday Cup

The Faraday cup is positioned in the middle of the main vacuum chamber (Figure 2.5) on a turn-table that allows for movement along or around four axes, two translation and two rotation axes. In the present setup we only make use of the translation axis z. The entrance aperture, usually circular with a diameter of 80 mm, is partially covered with aluminium foil to create a 20 mm-wide slit. For characterizing NIOS, the Faraday cup is moved along the z-axis to gain one-dimensional spatial scans. The Faraday cup

makes use of a repeller ring electrode that sits at the entrance aperture. The potential of the repeller ring is high enough to repel low energy secondary electrons from both entering and leaving the Faraday cup. Secondary electrons can be created whenever particles hit a surface. That can be somewhere outside of the Faraday cup and also inside. If the electrons created inside the cup were to leave the cup, they would distort the current measurement. It is connected to two ordinary 9 V-batteries that are connected in series, leading to a potential of $-18\,\mathrm{V}$ close to the ring and slightly less towards the center. Other power supplies have been tested, but the batteries turned out to be the best solution, because they introduced the least noise on the Faraday cup current.

The Faraday cup is connected to an analog Picoampere meter (Keithley Instruments, 610C Solid State Electrometer). The analog way of showing the value seemingly makes it difficult to read the value and one has to average visually. If the display would be digital, one could easily read off the number. However, the value would be an instantaneous sample out of a distribution, which has an unknown width. The reason to use a digital readout would be that the measurement can be automatized. A test measurement has shown that this leads to an increase of noise in the signal by several magnitudes, which is not acceptable. The analog Ampere meter is therefore used for the entire campaign, because it outperforms the digital one in terms of quality of measurement, even though it takes more time to conduct individual measurements.

Positioning of NIOS

NIOS is mounted on a second translation-table (see Figure 2.5, top panel, right side). Unlike the 4-axis turn-table, the second table only has one translation axis. The table makes it possible to move NIOS into and out of the beam. NIOS is oriented as can be seen in Figure 2.5. The charge exchange surface is closer to the inside of the vacuum chamber and the electrodes closer to the door of the chamber. When NIOS is not inside the beam profile, the total beam current itself can be measured with the Faraday cup, leading to the current I_{primary}. The distance between the exit of NIOS and the entrance of the Faraday cup is 300 mm.

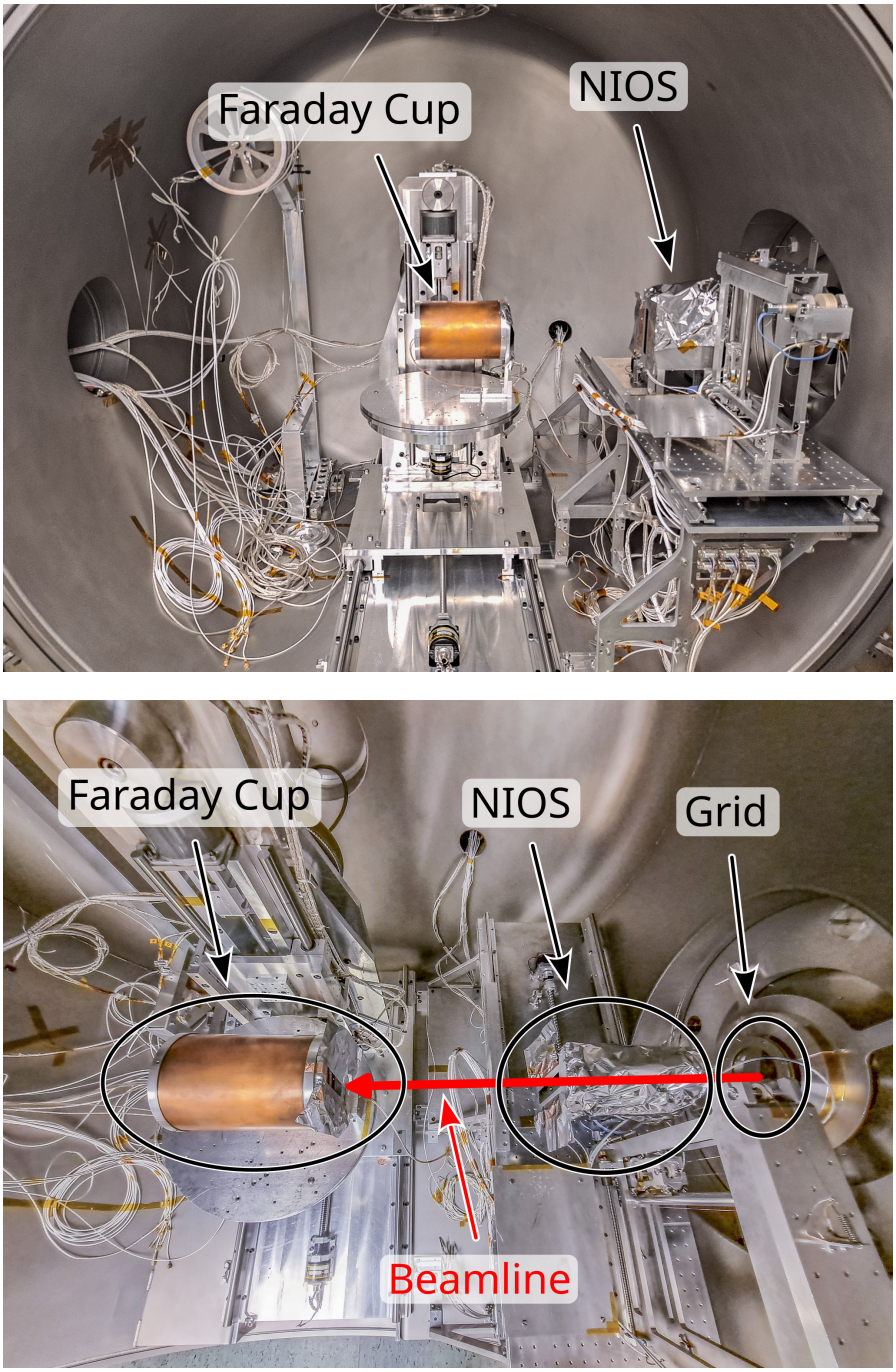

Figure 2.5: Photographs of the inside of the main vacuum chamber. *Top:* View from the front. The Faraday is placed on the turn-table in the center. NIOS is placed on the translation-table on the right. On the left there are multiple cables, some are used for this experiment, some are from previous ones. *Bottom:* Close-up top view. The circular aperture of the Faraday cup is partially covered by aluminium foil to create a 20 mm wide slit. NIOS is also covered in aluminium foil to increase its shadow and to block electrostatic stray fields coming from the electrodes within NIOS. At the far right, at the exit of the beam source, the grid is located.

2.3 Experimental Method

2.3.1 Starting up the Beam

At the beginning of every measurement campaign the beam needs to be switched on and adjusted. For that, several steps are necessary:

1. Set the filament current to 25 A. During this process the chamber pressure rises temporarily, therefore the current needs to be ramped up slowly. This heats up the filament, leading to thermal electrons.

2. Set the discharge arc voltage to approximately 90 V. This will lead to a discharge arc once the filament is hot enough.

3. Set the beam energy to the desired value by raising the floating potential of the source relative to ground.

4. Set the Einzel lens voltage to approximately 2 kV.

5. Set the ExB-filter voltage to the value that corresponds to the desired ion species. For a 1300 eV, H_2^+ beam the voltage needs to be around 620 V.

6. Set the ESA voltage to the value that corresponds to the desired ion species. For a 1300 eV, H_2^+ beam the voltage needs to be around 92 mV.

7. Set the negative potential of the electrodes inside NIOS. The potential is calculated by multiplying the beam energy by a predetermined factor $r_{\mathrm{NIOS}} = -0.1\,\mathrm{V\,eV^{-1}}$. That is −130 V for a 1300 eV beam.

As our primary ion species we use H_2^+, because of the higher beam intensity available for this species, compared to atomic H^+. H_2^+ dissociates to individual atoms upon scattering in NIOS. After charge exchange reactions with the scattering surface in NIOS, H^- is produced, one of the key species of interests for NILS. Many of the NILS calibration measurements were done with a H_2^+ primary beam.

When the beam has been switched on, after some time, usually in the range of minutes, a discharge arc forms and ions can be extracted. In order to optimize the beam intensity, NIOS is moved out of the beam and we measure the beam with the Faraday cup directly. Einzel lens voltage, ExB-filter voltage, and ESA voltage are fine-tuned until the Faraday cup current is maximized. Before any thorough measurements, we conduct a preliminary spatial scan of the primary beam. That means taking a couple of measurement with the Faraday cup of the primary beam at different locations. We inspect the shape and position of the beam and adjust it if need be. Since the origin of the z-axis is aligned with the edge of the NIOS body (compare Figure 2.3), the maximum of the primary beam should not be at $z = 0$. It should hit the entrance aperture of NIOS approximately in the center, therefore the beam intensity is maximized at $z = -10\,\mathrm{mm}$. It is important to widen the beam enough so it covers all of the NIOS entrance aperture. We therefore adjust the defocus lens voltage and monitor the grid current. While slowly increasing the

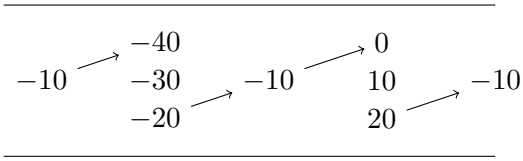

Figure 2.6: Measurement scheme for primary beam measurements. The numbers represent z-locations (in mm) at which the NIOS output beam is measurement in chronological order with duplicates at -10. Read column after column, from left to right.

defocus lens voltage, the grid current stays constant, until it starts to decrease. At this threshold, the beam has been widened to the diameter of the grid and a portion of the grid frame blocks the beam. We try to always find this sweet spot, when adjusting the beam. This way we also have the information of the divergence of the beam, which is later used for the data analysis.

2.3.2 Conducting a Spatial Scan

What we are interested in is the spatial profile of the output of NIOS. This quantity takes the form of the current density J_{FC}. We obtain the current density by taking current measurements with the Faraday cup at different locations and further processing. When the beam is set to a certain energy and the intensity is maximized, we conduct the spatial scan of the NIOS output beam. The measurement for one beam energy always consists of three measurement blocks. First the primary beam profile, then the NIOS output beam profile, and then the primary beam profile again. This allows for either compensation of time dependent variation of the shape of the beam profile or – in case changes are too significant – rejection of bad measurements.

First, the primary positive ion beam current I_{primary} is measured to gain a spatial scan of the primary beam. For that we move NIOS out of the beamline and the Faraday cup measures the positive ions directly. The measurement ranges from $z = -40\,\mathrm{mm}$ to $z = 20\,\mathrm{mm}$ with multiple measurements of the same location, namely $z = -10\,\mathrm{mm}$. The exact measurement scheme is shown in Figure 2.6. The duplicate measurements are used to correct for potential movement of the beam center.

Then, we move NIOS back into the beamline and perform a regular spatial scan of the NIOS output. Figure 2.7 shows the chronological measurement scheme. Like for the primary beam, we take duplicate measurements to have a proxy for the time dependent change of beam intensity. Last, we repeat the measurement of the primary beam.

For each location we measure three quantities: The *grid current* I_{grid}, which comes from the 90 % transparent grid directly at the exit of the ion source. It is read off from a digital Ampere meter. The *Faraday current* I_{FC}, which comes from the Faraday cup. It is read off from the analog Ampere meter. And for each I_{FC} measurement, the *uncertainty* of I_{FC} is estimated in the form of $2\sigma_{\mathrm{FC}}$. It comes from noise in the signal leading to statistical needle movement of the analog Ampere meter. For the grid current measurements we set a constant, relative uncertainty of 10 %.

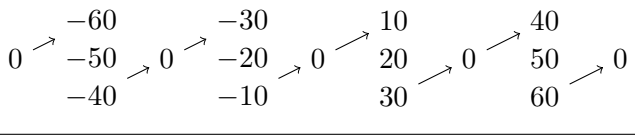

Figure 2.7: Measurement scheme for NIOS output beam. The numbers represent z-locations (in mm) at which the NIOS output beam is measurement in chronological order with duplicates at 0. Read column after column, from left to right.

2.3.3 Data Processing

When the measurement for one energy is finished, there are three tables:

1. Primary beam profile before,
2. NIOS profile,
3. and primary beam profile after.

Each table contains z in [mm], I_{grid} in [A], I_{FC} in [A] and $2\sigma_{\text{FC}}$ in [A]. To keep track of the different data processing steps, we will denote the unprocessed, measured Faraday cup current with I^{**}_{FC}.

Accounting for the Faraday Cup Aperture

The Faraday cup has a slit-shaped aperture with an area

$$A_{\text{FC}} = 20\,\text{mm} \cdot 80\,\text{mm}. \tag{2.1}$$

Every current measurement is therefore an integration over the slit area. In order to account for that, every current measurement of the Faraday cup I^{**}_{FC} is divided by the area, such that

$$J^{**}_{\text{FC}}(z) = \frac{I^{**}_{\text{FC}}(z)}{A_{\text{FC}}} \tag{2.2}$$

The current effectively becomes a current density J with the unit [A/mm^2] and is independent of the slit width.

First Correction

The first step in correcting the data for time dependence is to account for the varying grid current I_{grid}. This is done by picking the first I_{grid} measurement of the first primary beam profile, denoted by $I_{\text{grid,0}}$ and applying the following formula to the uncorrected Faraday current density J^{**}_{FC} of all three measurement blocks – primary beam profile before, NIOS profile, and primary beam profile after:

$$J^{*}_{\text{FC}}(z) = \frac{I_{\text{grid,0}}}{I_{\text{grid}}(z)} \cdot J^{**}_{\text{FC}}(z). \tag{2.3}$$

Quantities denoted with * are corrected for the grid current. If the grid current increases over time, the fraction becomes smaller, thus decreasing the effective Faraday current density J^*_{FC}. Vice versa for a decrease of grid current density.

Second Correction

After this correction, it is still possible for the duplicate measurements at $z = -10\,\mathrm{mm}$ or $z = 0\,\mathrm{mm}$ to differ. Therefore another correction is applied. First, we put the Faraday current densities of the duplicates $J_{\mathrm{FC,dupl}}$ into a table with their respective index n in the measurement sequence, like

n	0	3	6
$J^*_{\mathrm{FC,dupl}}$	J_0	J_3	J_6

Then we linearly interpolate the missing indices and currents such that there is a duplicate measurement for every index position. This results in the table

n	0	1	2	3	4	5	6
$J^*_{\mathrm{FC,dupl}}$	J_0	J_1	J_2	J_3	J_4	J_5	J_6

Now the effective Faraday current density can be corrected further, according to

$$J_{\mathrm{FC}}(z) = \frac{J^*_{\mathrm{FC,dupl,0}}}{J^*_{\mathrm{FC,dupl}}(z)} \cdot J^*_{\mathrm{FC}}(z), \tag{2.4}$$

with $J^*_{\mathrm{FC,dupl,0}}$ being the first of the duplicate measurements. If after some time the measured currents of the duplicates vary, the whole spatial scan gets anti-proportionally adjusted.

Fitting the Data

We assume that the output of NIOS consists of a Gaussian-shaped ion peak and some kind of a linear background. The data are therefore fitted using a least-squares method. We fit a combination of a Gauss and a linear function

$$f_{\mathrm{fit}}(z, A, z_0, \sigma, m, t) = A \cdot \exp\left(-\frac{1}{2}\,\frac{(z - z_0)^2}{\sigma^2}\right) + m\,z + t, \tag{2.5}$$

with A being the amplitude, z_0 the center and σ the standard deviation of the Gauss. m is the slope and t the y-intersect of the linear part. These variables are the fit-parameters, which are optimized to describe the data as good as possible.

Deconvolution

The object of interest is the spatial profile of the NIOS output current density J_{FC}, in the following called the true signal S_{true}. By scanning over S_{true} with the Faraday cup we automatically perform a convolution of S_{true} and the aperture of the Faraday cup, denoted P_{FC}. In the context of the scanning process the aperture has the shape of a boxcar function. A boxcar function is zero over the entire argument range except for a single interval where it is equal to a constant. The function has a width of 20 mm and a height of 1/20 mm. The true signal therefore becomes

$$S_{\mathrm{convolution}} = S_{\mathrm{true}} * P_{\mathrm{FC}}, \tag{2.6}$$

where $*$ is the convolution operator. In order to retrieve the original signal S_{true}, one has to perform a deconvolution. The inverse nature of the problem makes deconvolving a difficult task. The convolution can be understood as a smoothing of the signal, which leads to information-loss that cannot be undone simply. We therefore use a reformulation of the problem in order to avoid having to perform the deconvolution.

The measurement yields discrete data points D_{measured} which are used to fit Equation 2.5, leading to the continuous signal D_{fit}. Now $S_{\mathrm{convolution}}$ and D_{fit} can be identified as describing the same object.

$$D_{\mathrm{measured}} \xrightarrow{f_{\mathrm{fit}}} D_{\mathrm{fit}} \quad \hat{=} \quad S_{\mathrm{convolution}} = S_{\mathrm{true}} * P_{\mathrm{FC}}. \tag{2.7}$$

D_{fit} is known. It is given by the fitting process of the measured data. P_{FC} is known. It comes from the Faraday cup aperture width. S_{true} is partly known. Since $S_{\mathrm{convolution}}$ corresponds to D_{fit}, both are assumed to have the same underlying character, meaning a combination of Gauss and linear part (Equation 2.5). Since we know that the convolution has a Gaussian character and one of the convoluted objects (P_{FC}) is a boxcar-function, we can infer that S_{true} must also be of Gaussian nature. Hence, the true signal can be expressed with f_{fit} as well.

We define a second fit function

$$f_{\mathrm{fit,convolution}}(z, A, z_0, \sigma, m, t) = f_{\mathrm{fit}}(z, A, z_0, \sigma, m, t) * P_{\mathrm{FC}}, \tag{2.8}$$

where the fit parameters are the variables of the Gauss-linear function inside the convolution. The fitting algorithm adjusts $f_{\mathrm{fit,convolution}}$ such that it closely matches D_{fit}.

$$D_{\mathrm{fit}} \xrightarrow{f_{\mathrm{fit,convolution}}} D_{\mathrm{fit,convolution}} \quad = \quad S_{\mathrm{convolution}} \tag{2.9}$$

The resulting fit parameters of $D_{\mathrm{fit,convolution}}$ are then used to retrieve S_{true}. With this reformulation of the problem the deconvolution becomes a simpler convolution and fitting task, which can be done without having to take care of any lost information or introduction of noise.

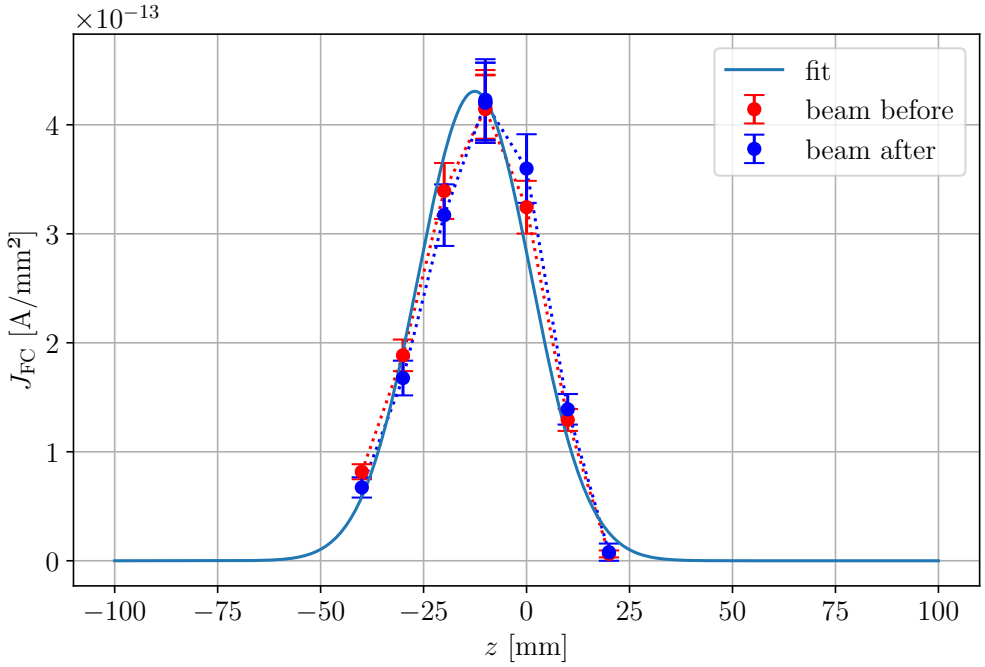

Figure 2.8: Current density profiles for primary beams before (red circles) and after (blue circles) NIOS measurement. 450 eV beam energy. Gaussian fit applied to mean density at every z-location.

Normalization

The product of the characterization should be as independent of the experimental setup as possible, otherwise aspects like the measurement device or the beam intensity influence the result. The primary beam intensity of the plasmatron source is dependent on many different parameters and can vary to a certain degree from day to day. In order to mitigate the dependence on the primary beam, we normalize J_{FC} with the primary beam current $I_{primary,NIOS}$ that actually enters NIOS.

We obtain $I_{primary,NIOS}$ by integrating the current density over the entrance area of NIOS. Since the spatial scans were only performed in one dimension, we need to estimate the shape of the beam in the remaining direction. In the calibration facility this direction is denoted w. Since scans were conducted in z, we can get the shape of the beam in this direction by applying a Gaussian fit to the measured data. As an example for one energy (450 eV), Figure 2.8 shows both primary beams – before and after the NIOS measurement – as well as the Gaussian fit. For every z-value where measurements exist, the mean of all current densities is taken. The Gaussian is then fitted to the mean density at every z, resulting in $J_{primary,fit}$.

If we assume the beam is circular symmetric, we can describe it with a symmetric

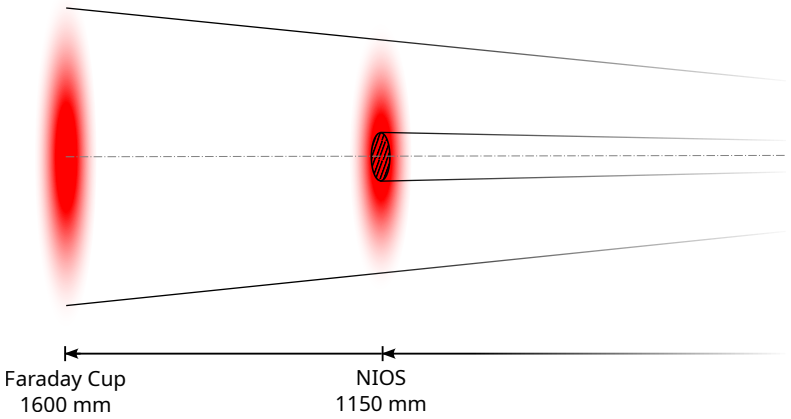

Figure 2.9: Primary beam densities in red at different locations. Entrance of NIOS is indicated by the striped area.

two-dimensional Gauss function

$$J_{\text{primary,2D}}(z,w) = A \cdot \exp\left(-\frac{1}{2}\frac{(z-\mu)^2}{\sigma^2}\right) \cdot \exp\left(-\frac{1}{2}\frac{(w-\mu)^2}{\sigma^2}\right), \tag{2.10}$$

where A, μ, and σ come from the Gauss fit for the z-direction. Both exponential terms share the same center μ and width σ.

Note that $J_{\text{primary,2D}}$ – with the parameters μ and σ – expresses the current density at the location of the Faraday cup (compare to Figure 2.9). We need to calculate the density profile at the location of NIOS. At a distance from the Faraday cup $d_{\text{FC}} = (1.60 \pm 0.04)\,\text{m}$ and at a distance from NIOS $d_{\text{N}} = (1.15 \pm 0.04)\,\text{m}$ can the source be considered to be a point source. If we denote the parameters relative to the Faraday cup location with $_{\text{FC}}$ and relative to the NIOS location with $_{\text{N}}$, then the scaled Gauss parameters can be expressed as

$$\sigma_{\text{N}} = \sigma_{\text{FC}} \frac{d_{\text{N}}}{d_{\text{FC}}} \tag{2.11}$$

$$A_{\text{N}} = A_{\text{FC}} \frac{\sigma_{\text{FC}}}{\sigma_{\text{N}}}. \tag{2.12}$$

With the current density $J_{\text{primary,2D}}$ at the location of NIOS, we can calculate the current $I_{\text{primary,NIOS}}$ that enters NIOS. Under the assumption that the beam hits the entrance of NIOS in the center ($\mu = 0$), the current becomes

$$I_{\text{primary,NIOS}} = \int_{-Z/2}^{Z/2}\int_{-W/2}^{W/2} J_{\text{primary,2D}}(z,w)\,\mathrm{d}w\,\mathrm{d}z \tag{2.13}$$

$$= \int_{-Z/2}^{Z/2}\int_{-W/2}^{W/2} A_{\text{N}} \cdot \exp\left(-\frac{1}{2}\frac{z^2}{\sigma_{\text{N}}^2}\right) \cdot \exp\left(-\frac{1}{2}\frac{w^2}{\sigma_{\text{N}}^2}\right) \mathrm{d}w\,\mathrm{d}z. \tag{2.14}$$

The integration intervals correspond to the NIOS entrance dimensions of $W \cdot Z = 30\,\text{mm} \cdot 15\,\text{mm}$. As the integrand is symmetric in z and w, it does not matter which dimension is used for which integration. Finally, the normalized current density of NIOS is then

$$J_{\text{FC,norm}}(z) = \frac{J_{\text{FC}}(z)}{I_{\text{primary,NIOS}}} \tag{2.15}$$

This quantity has the unit $[1/\text{mm}^2]$. It is independent of the primary beam current present during the characterization. In order to get back to a real current density, one simply has to multiply by the current that enters NIOS.

Uncertainties

The uncertainties of I_{grid} and I_{FC}^{**} mentioned in subsection 2.3.2, and the uncertainties of the measured lengths in this section, are propagated through all correction and normalization steps. Since the character of the uncertainties is assumed to be Gaussian, it is legitimate to use Gaussian error propagation for that.

2.4 Characterization Results

Let us remember what the goal of the characterization is. The characterization describes and quantifies the output of NIOS. First, this is needed for the calibration of NILS. Second, we use it to tune the simulation of NIOS with it to then have a more accurate model for the optimization process.

In Figure 2.10 the spatial scan of the NIOS output beam for a primary beam energy of 450 eV is depicted. The data in this plot are corrected according to subsection 2.3.3, but they are not normalized to the primary beam in order to show the absolute values once. Because of the second correction step, which corrects the variation of the duplicate measurements, the duplicates lay on top of each other and multiple error bar caps are visible for $z = 10\,\text{mm}$. The floor height and the peak height are visualized. Floor height refers to the value of the linear part of f_{fit} at the z-location of the minimum of the fit. Peak height refers to the value of the Gaussian part at the location of the minimum, in other words A. We determine the heights for every primary beam energy measured.

The spatial scan of the NIOS output is done for the energies 450 eV, 600 eV, 900 eV, 1300 eV, 2000 eV, 3000 eV, and 5000 eV. Figure 2.11 displays these measurements, as well as the corresponding fits. Here, the normalized current density is used in order to compare different energies to each other. By normalizing the current density, we remove the dependency on the beam intensity from the measurements. As discussed earlier, the ion source has different modes for high and low energies and 1300 eV can be used in either. The energies 1300 eV and lower use the low-energy mode and the rest use the high-energy mode.

For each beam energy, the fitted peak height is depicted in Figure 2.12. Note that the y-axis shows negative $J_{\text{FC,norm}}$. We can see a trend in this plot. There seems to be a higher negative current density for higher energies.

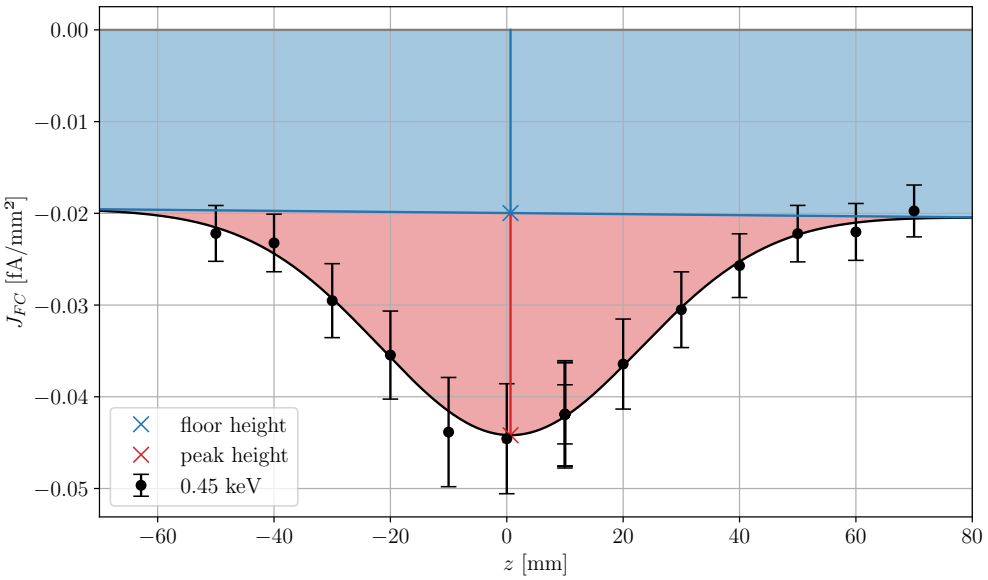

Figure 2.10: Spatial scan of NIOS output for 450 eV. The corrected, unnormalized Faraday cup current density in [fA/mm^2] is depicted. The measurement points and the fit through them are shown in black. The red area shows the Gaussian part of fit-function and blue shows the linear part. The crosses show the values for both parts corresponding to the location of the minimum.

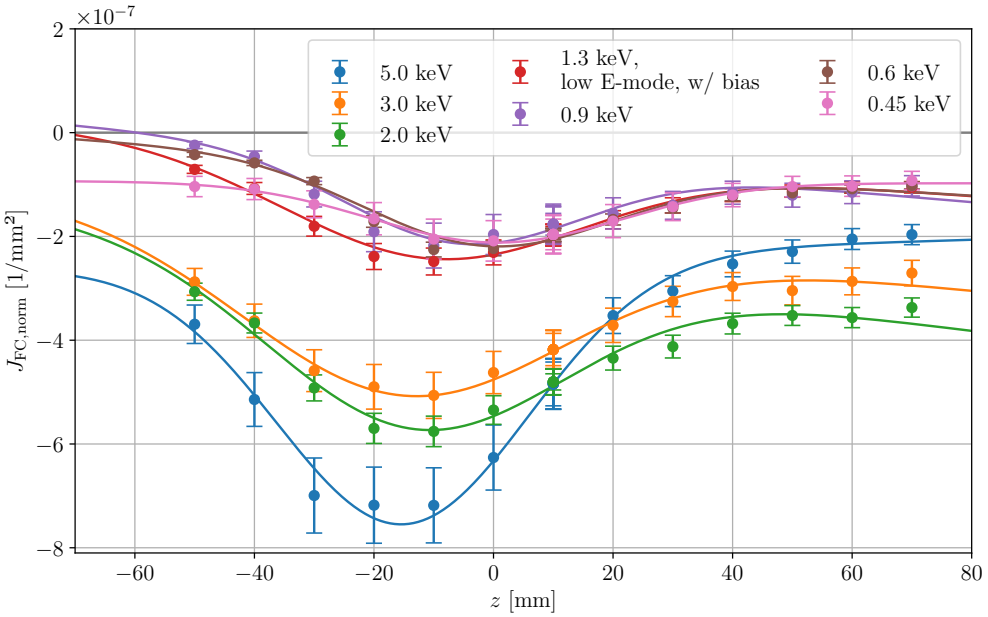

Figure 2.11: Spatial scan of NIOS output for different energies. The corrected and normalized Faraday cup current density is plotted. Measurement points and corresponding fit have the same color.

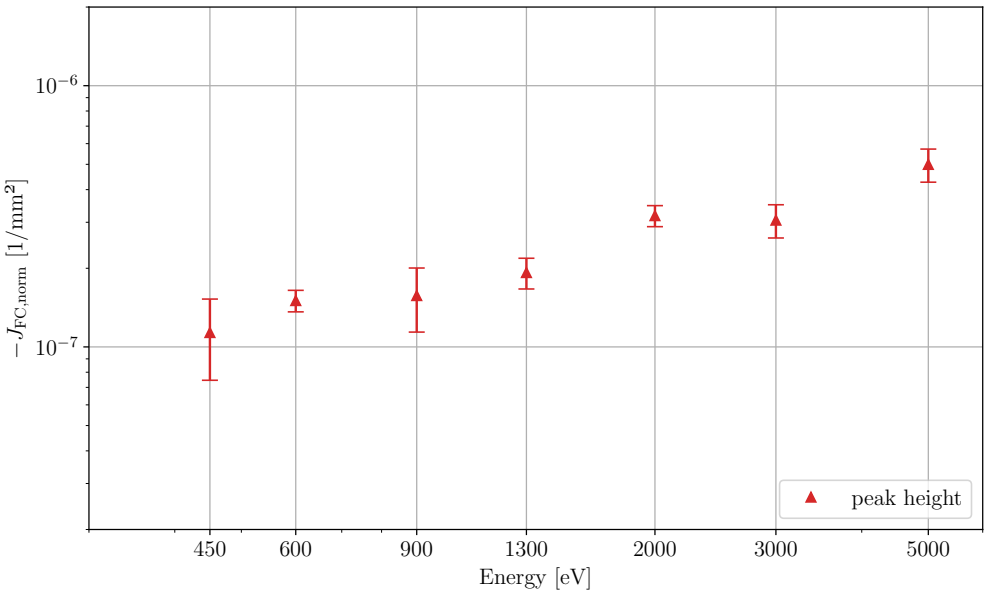

Figure 2.12: Peak height for different energies. The y-axis shows negative $J_{\mathrm{FC,norm}}$.

During the measurement campaign, measurements for the beam energy 1300 eV were done in both ion source modes, high-energy and low-energy. We noticed that the results differ depending on the source configuration. Figure 2.13 illustrates the influence of the ion source configuration on the measurements. The beam energy is constant at 1300 eV. One measurement is done in high-energy mode, the rest in low-energy mode. For the low-energy mode the bias voltage is varied from 0 kV to 5.22 kV. For a higher bias voltage the current densities seem to decrease.

For the four measurements in low-energy mode, the floor height and peak height are shown in Figure 2.14. Here it becomes apparent that it is the floor that depends on the bias voltage. The peak height stays constant, as the constant fit shows.

If we now return to Figure 2.11, remove the floor population and only plot the Gauss part of f_{fit}, we get Figure 2.15. These are the characterization curves provided for the NILS calibration. The parameters of the curves are given in Table 2.1. The errors on the parameters result from the fitting process, taking into account the errors on the individual measurement points.

2.5 Characterization Discussion

2.5.1 Floor population

As visualized in Figure 2.10, for fitting the data we use a combination of a Gauss part and a linear part. We assume that the Gauss part is due to negative ions in the beam. This assumption is confirmed by measurements from the NILS instrument, which show a negative ion peak at that location.

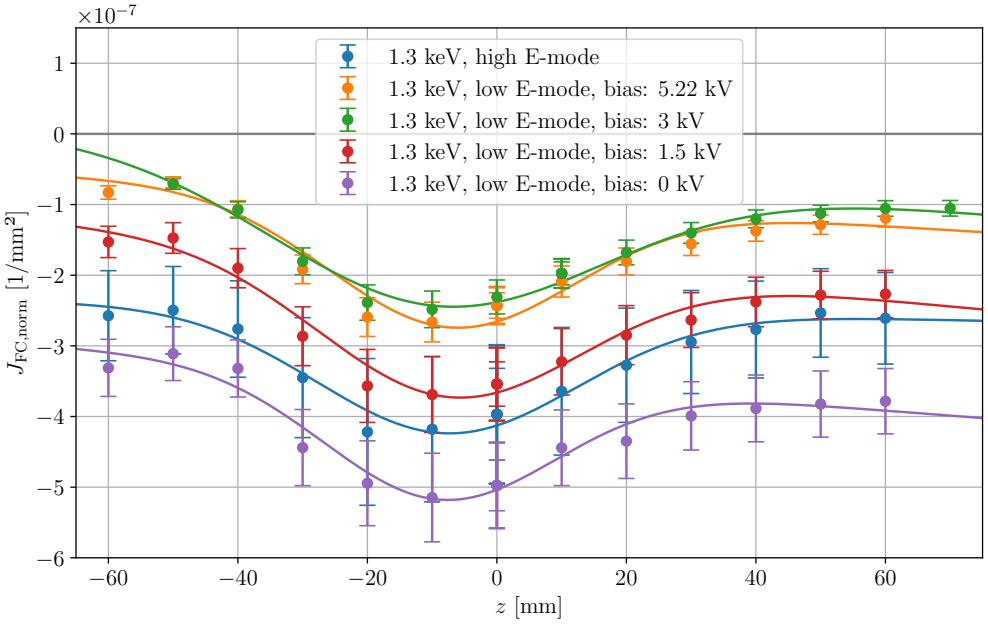

Figure 2.13: Spatial scans of NIOS output. The beam energy is constantly 1300 eV. Different ion source settings are used, both high-energy and low-energy mode with varying ExB bias voltage.

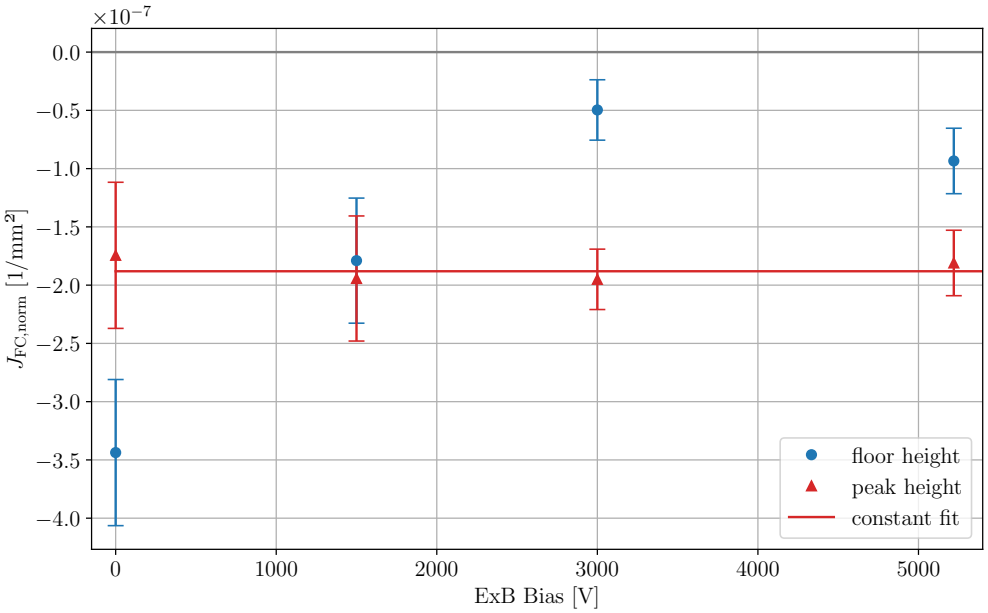

Figure 2.14: Floor height and peak height for different ExB bias voltage. The beam energy is 1300 eV.

Table 2.1: Parameters for spatial NIOS profiles. The errors originate in the fitting process.

Energy [eV]	A [10^{-7}/mm^2]	z_0 [mm]	σ [mm]
5000	-5.15 ± 0.46	-15.2 ± 1.7	21.1 ± 2.4
3000	-3.12 ± 0.56	-15.5 ± 3.0	26.7 ± 4.2
2000	-3.25 ± 0.53	-13.4 ± 2.9	24.7 ± 4.3
1300	-1.99 ± 0.16	-10.5 ± 1.7	25.0 ± 2.6
900	-1.65 ± 0.14	-5.7 ± 1.7	19.9 ± 2.7
600	-1.56 ± 0.09	-1.2 ± 1.5	20.8 ± 2.0
450	-1.17 ± 0.04	0.5 ± 0.8	21.0 ± 1.0

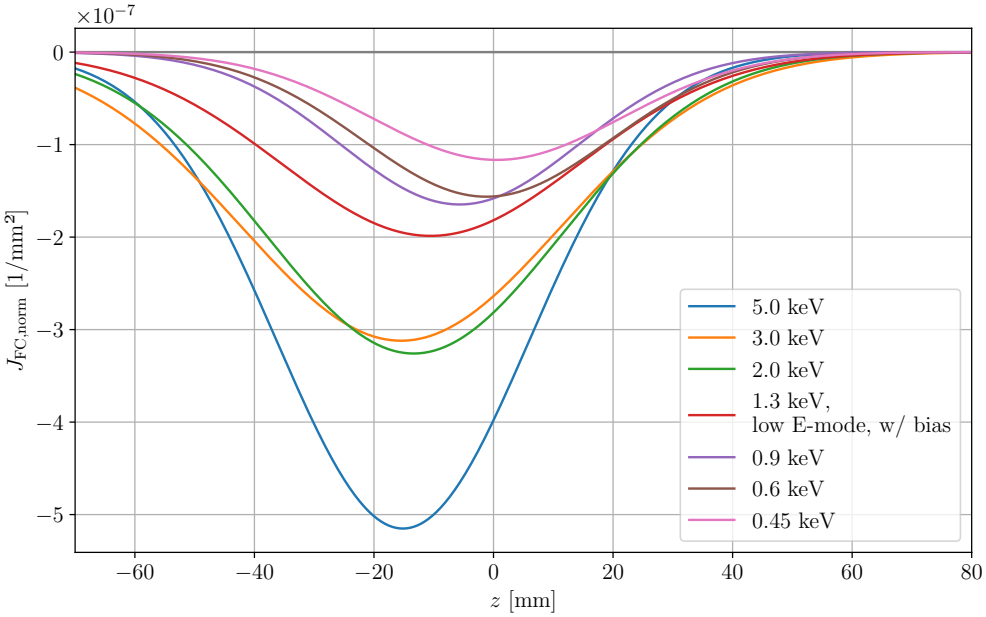

Figure 2.15: Fit funcitons to the spatial scans of NIOS output with floor removed.

In order to explain the negative floor, multiple theories come to mind. The first one being low-energy secondary electrons. An abundance of those kind of electrons can be found everywhere in the vacuum chamber. They are the result of surface interactions of the beam and the higher the beam energy, the higher the secondary electron yield. Secondary electrons usually have an energy around 2 eV (Seiler, 1983) and are therefore prevented from entering the Faraday cup by the repeller ring, which has a potential of -18 V. Yet, the electric field created by the ring is not homogeneous and has a lower potential in the center. Because of that and because the electrons can gain energy by being accelerated in electric fields, low-energy electrons are a potential cause for the floor. However, measurements of the Faraday cup current, while ramping up the repeller potential from 0 V to 45 V, showed no low-energy electron population besides the expected

electrons of about 2 eV to 8 eV, which were already repelled in the first setup.

Another explanation could be secondary electrons originating from NIOS, meaning electrons that have an energy corresponding to the NIOS inner electrode voltage. These would arrive at the Faraday cup from an energy dependent direction due to the effect of Earth's magnetic field. This kind of population has been observed by NILS.

Last, the negative floor could also be due to parasitic leakage currents across insulator surfaces from any elements that are on high voltage in the ion source. Such currents could easily reach the pA range used in our measurements given that high voltages of several kV are used in the ion source. A possible candidate sourcing such a current is the ExB bias voltage.

2.5.2 Influence of ExB Bias Voltage

Since the 1300 eV measurements display differences depending on the ion source configuration, additional measurements for constant beam energy are conducted. The ExB bias voltage is varied from 0 kV to 5.22 kV and the Faraday cup current is measured (Figure 2.13). When we look at the two components of the signal, shown in Figure 2.14, we see a clear dependence on the bias voltage for the floor population and a clear independence on it for the ion population. How exactly this dependence comes to be is not fully understood. The results of this work are not influenced by it, because in subsection 2.5.3 we remove the floor population to isolate the signal of interest, the negative ions. For previous and future measurements, however, it is valuable to know that such a dependence exists.

2.5.3 Characterization Curves

The characterization curves, meaning the fully processed spatial scans of NIOS with the floor population removed, are shown in Figure 2.15 (and the curve parameters in Table 2.1, respectively). From looking at the figure, we can see that the negative current density increases for higher beam energies. It seems that during the scattering process more negative ions are emitted the higher the primary beam energy is. This hypothesis indeed makes sense, when we compare ion peak heights for different energies from Figure 2.12 and plot them together with negative ionization efficiency data from Wieser (2005). This is depicted in Figure 2.16. Note that the two quantities are not equal. The ionization efficiency is a measure for how effectively negative ions are emitted upon scattering. The current density, however, entails only ions that managed to escape NIOS. The number of ions leading to the current density are therefore just a subset of the total number of ions. But what we can infer from this figure is that a proportionality between primary beam energy and negative ion yield is observed in the external data as well as in the measurements for this work. We consider the characterization validated and hand over the data to the NILS calibration.

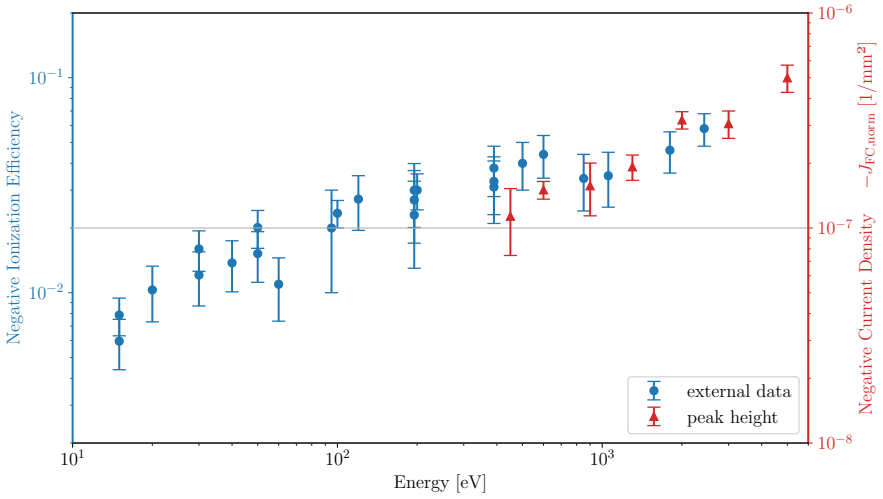

Figure 2.16: Comparison of measured peak height (red) and ionization efficiency from scattering hydrogen off several diamond surfaces (green) taken from Wieser (2005, p. 198).

3 Simulation

3.1 Simulation Objective

The already available charge conversion particle source NIOS was designed by simulating physical key characteristics such as the geometry of the box and the electrostatic field. Particles starting at the conversion surface with a certain energy and velocity direction are then subject to the field, resulting in an electric force which changes their trajectories if their charge is non-zero. The simulation was used to optimize the geometry and the electric field such that many negative ions and few of the other particles can reach the detection surface outside of NIOS.

The second task of this thesis is to improve the simulated NIOS-particle interaction substantially, in order to improve the quality of the geometry optimization in the following step. The optimization evaluates various simulation runs and the more accurately the simulated particle behavior represents reality, the more effective the optimization becomes in the end. However, trying to fully represent reality can be counterproductive, because it leads to unnecessary complexity and excessive computational time. Thus, making appropriate assumptions and simplifications is essential.

3.2 Simulation Software

3.2.1 Definition of Potential Arrays

The software utilized for simulating NIOS is SIMION (Dahl, 2000). The software package has the capability to simulate ion optics problems with 2D symmetrical and 3D asymmetrical electrostatic and magnetic potential arrays (PAs).

A potential array is defined as a set of equi-distant points, each having a potential and a type. As described in the SIMION user manual by Manura and Dahl (2008), the potential arrays define the geometry of electrodes (or magnetic poles). The electric potential is given in Volts and the magnetic potential in Mags, which is SIMION's own unit to handle magnetic potential fields. The type of each element in the array can be either electrode/magnetic pole or non-electrode/non-pole. It can never be both electrode and magnetic pole at the same time. An electrode/magnetic pole is a solid and particles cannot travel there. The opposite is true for a non-electrode/non-pole. For using both electrodes and magnetic poles in the same volume, two or more PAs need to be superimposed. An example 2D potential array is depicted in Figure 3.1. Dots represent free space through which particles can traverse. Squares are set to be electrodes/poles. Groups of squares form the shape of electrodes or poles. When particles hit electrodes or leave the defined area, they are removed from the simulation and counted as "splat".

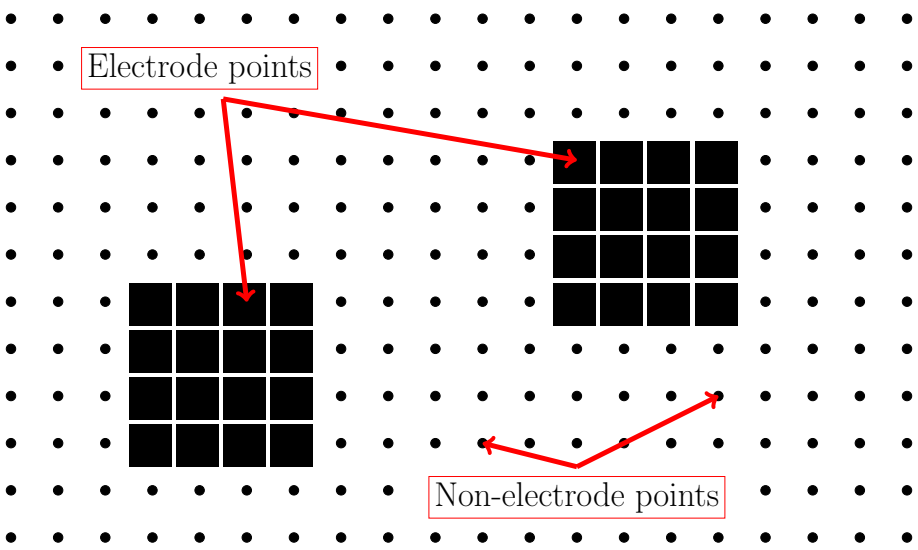

Figure 3.1: Schematic two-dimensional potential array as used by SIMION. Dots represent non-electrode, squares represent electrode.

SIMION has two classes of potential arrays, basic potential arrays (`.PA` files) and fast adjust definition arrays (`.PA#` files). A basic potential array is defined as described above and processed by SIMION's `refine` function to calculate the potential at each point in space via the Laplace equation. The fast adjust definition array differs by not having the electrode potentials defined explicitly. The potentials are defined after refining. The Laplace equation is solved independently for each electrode and the solutions are then linearly combined due to the additive property of the Laplace equation. This allows for fast adjusting without having to re-refine from scratch every time a potential is changed.

3.2.2 Potentials and Gradients

The potentials within the electrodes are usually set by the user and the potentials in the space between the electrodes are determined by solving the Poisson equation under the assumption of having zero space charge ρ, which results in the Laplace equation

$$\boldsymbol{\nabla}^2 V = \boldsymbol{\nabla} \cdot \boldsymbol{\nabla} V = -\boldsymbol{\nabla} \cdot \mathbf{E} = 0. \tag{3.1}$$

This is the equation used by SIMION to evaluate the electrostatic and static magnetic potential field V at every point in the defined space. In order to receive electrostatic and static magnetic fields from the potentials, one has to consider the gradient of the potentials.

Electric Potential Arrays

Electric potentials in the PAs are always given in Volts. Since the distances between points in the PA are given in grid units (gu), the electric PAs are scaled with a user specified scaling factor k_E which allows for the grid to represent physical lengths. Unless specified differently, this factor is 1 mm/gu. The gradient of the potential is computed as

$$\begin{aligned} -\mathbf{E} = \boldsymbol{\nabla} V = \boldsymbol{\nabla} V_{PA} \cdot \frac{1}{k_E} \\ [\mathrm{V/mm}] = [\mathrm{V/gu}] \cdot [\mathrm{gu/mm}]. \end{aligned} \tag{3.2}$$

Magnetic Potentials

In the magnetic case the situation is more complex. When dealing with electrostatics we are used to think of scalar potential fields. In magnetics it is much more common to think of and measure flux density $\mathbf{B}$ (in units Tesla or Gauss). SIMION is not a magnetic circuit program and magnetic potential arrays need to be provided by the user. SIMION can only refine scalar potential arrays. This problem is addressed by defining magnetic potentials in the unit Mags, which is defined as Gauss times grid unit (G gu) and the gradient is then simply given in Gauss. Defining it in units G mm would lead to problems when scaling the array instance. Thus, SIMION approximates the magnetic flux density $\mathbf{B}_{\mathrm{PA}}$ in the array instance to be the gradient of the scalar magnetic potential Φ_{M} array such that

$$\begin{aligned} \mathbf{B}_{\mathrm{PA}} = \boldsymbol{\nabla} \Phi_{\mathrm{M}} \\ [\mathrm{G_{PA}}] = [\mathrm{Mags/gu}]. \end{aligned} \tag{3.3}$$

Here, $\mathrm{G_{PA}}$ denotes Gauss in the reference frame measured in grid units.

SIMION furthermore introduces a scaling factor ng as a property of magnetic PAs. This allows for a direct relation between the units Mags and Gauss in the reference frame measured in millimeters. ng is called pole gap scaling factor and is set equal to the distance between two poles. For example, if the distance between to poles is 100 gu, then ng is set to 100. This roughly translates Mags to Gauss in the millimeter reference frame, such that the flux density is

$$\begin{aligned} \mathbf{B} = \mathbf{B}_{\mathrm{PA}} \cdot ng \\ [\mathrm{G}] = [\mathrm{G_{PA}}] \cdot [ng]. \end{aligned} \tag{3.4}$$

In SIMION the $\mathbf{B}$ field is defined to point from higher to lower magnetic potential. It needs to be pointed out that some magnetic fields cannot be expressed as scalar potentials but rather as vectors. Unlike electrodes, in general magnetic poles do not have the same potential across their surface. One should check whether this has a significant impact on the simulation.

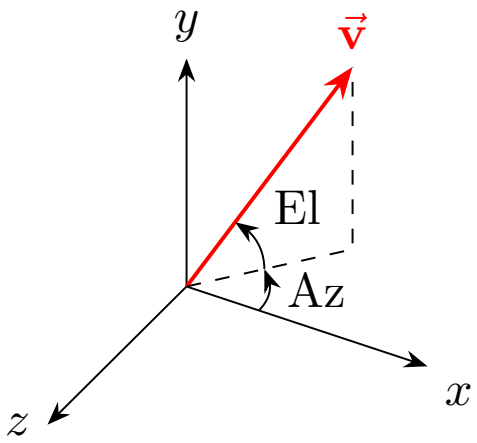

Figure 3.2: Coordinate system as defined by SIMION with azimuth and elevation angle.

3.2.3 Defining Particles

In order to fly ions they need to be defined first. In particular, the parameters mass, charge, kinetic energy, starting location and direction are of interest. The direction can be given in terms of a vector in x, y and z, or azimuth and elevation angle, as depicted in Figure 3.2. The length of the velocity vector is defined via the kinetic energy.

3.2.4 Fundamental Ion-optical Concepts

Ion optics play a crucial role for the understanding of ion trajectory formation. In order to give a basic understanding of ion optics, some key concepts will be laid out, following Manura and Dahl (2008).

Influence of an arbitrary Force

Newton's second law describes how particles move, when subject to a force:

$$\mathbf{F} = m\,\mathbf{a} \tag{3.5}$$

with m being the mass and a the acceleration.

When a particle is accelerated by this force over a distance r, work W is being done

$$W = \int \mathbf{F} \cdot \mathrm{d}\mathbf{r}, \tag{3.6}$$

which changes the particle's kinetic energy.

Influence of Point Charges and Electric Fields

The forces acting between charged particles with the charges Q_i are given by Coulomb's law for two particles

$$\mathbf{F}_\mathrm{e} = \frac{1}{4\pi\,\varepsilon_0}\,\frac{Q_i\,Q_j}{|\mathbf{r}|^2}\,\hat{\mathbf{r}}, \tag{3.7}$$

and for multiple particles

$$\mathbf{F}_\mathrm{e} = \frac{1}{4\pi\,\varepsilon_0}\,Q_i \sum_n \frac{Q_n}{|\mathbf{r}_n|^2}\,\hat{\mathbf{r}}_n, \tag{3.8}$$

with ε_0 being the vacuum permittivity and $\mathbf{r}$ the distance between two particles.

An electric field $\mathbf{E}$ can be understood as the cause of the force $\mathbf{F}_E$ on a charged particle:

$$\mathbf{F}_\mathrm{E} = -e\,\mathbf{E}, \tag{3.9}$$

with e being the elementary charge.

Starting from Equation 3.5, one receives the acceleration on a charged particle in an electric field

$$\mathbf{a}_\mathrm{E} = \frac{\mathbf{F}_\mathrm{E}}{m} = -\frac{e\,\mathbf{E}}{m}. \tag{3.10}$$

The acceleration by an electric field changes the kinetic energy of the particle.

Influence of Magnetic Fields

If the particle is located in a magnetic field $\mathbf{B}$ and its velocity $\mathbf{v}$ is non-zero, it will be subject to the force

$$\mathbf{F}_\mathrm{M} = e\,\mathbf{v} \times \mathbf{B}. \tag{3.11}$$

This results in an acceleration to the particle of

$$\mathbf{a}_\mathrm{M} = \frac{\mathbf{F}}{m} = \frac{e}{m}\,\mathbf{v} \times \mathbf{B}. \tag{3.12}$$

One can see that the acceleration is always perpendicular to both velocity of the particle and magnetic field. Therefore a static magnetic field results in a change of the particles direction, but not its kinetic energy. That would require a movement along the magnetic field lines, not perpendicular to them.

In the general case, the motion of a charged particle in electrostatic and static magnetic fields can be described by the Lorentz force

$$\mathbf{F}_\mathrm{L} = q\,(\mathbf{E} + \mathbf{v} \times \mathbf{B}). \tag{3.13}$$

Refraction in Ion Optics

When electric or magnetic fields act on an ion and result in forces perpendicular to the velocity, bending the trajectory of the ion, we can consider that similar to refraction in classic optics.

The electrostatic radius of refraction can be calculated by setting the perpendicular electrostatic force equal to the centripetal force

$$\begin{aligned} F_{\mathrm{E},\perp} &= F_{\mathrm{c}} \\ -e\,E_{\perp} &= m\,\frac{v^2}{r_{\mathrm{E},\perp}} \\ r_{\mathrm{E},\perp} &= -\frac{m}{e}\,\frac{v^2}{E_{\perp}}. \end{aligned}$$

The radius is proportional to the kinetic energy of the particle $E_{\mathrm{kin}} = mv^2/2$. We can plug in the energy and yield

$$r_{\mathrm{E},\perp} = -\frac{2}{e\,E_{\perp}}\,E_{\mathrm{kin}} \tag{3.14}$$

Therefore, in electrostatic fields only, all ions with the same starting location, direction and kinetic energy per elementary charge have the same **mass independent** trajectory. The magnetic radius of refraction for a static field can be calculated analogously

$$\begin{aligned} F_{\mathrm{M},\perp} &= F_{\mathrm{c}} \\ B_{\perp}\,e\,v &= m\,\frac{v^2}{r_{\mathrm{M},\perp}} \\ r_{\mathrm{M},\perp} &= \frac{m}{e}\,\frac{v}{B_{\perp}}. \end{aligned}$$

Here we can also plug in the kinetic energy leading to

$$r_{\mathrm{M},\perp} = \frac{\sqrt{2\,m}}{e\,B_{\perp}}\,\sqrt{E_{\mathrm{kin}}}. \tag{3.15}$$

Therefore, in static magnetic fields only, all ions with the same starting location, direction and kinetic energy per elementary charge have the same **mass dependent** trajectory. Because of the square root proportionality in the magnetic radius, the magnetic refractive power is superior for high ion velocities, meaning for equal energies, the magnetic refractive radius is smaller than the electric.

3.3 Simulation Models

At the beginning of this work two different geometry models for the simulation were provided. The first one shall be called the optimization model (OptM) and the second one the STL model (STLM). In Figure 3.3 the different development steps of the simulation are shown. Originally, the optimization model started with the first version of the geometry and implemented physics (Geometry V0 and Physics V0). The mechanical workshop of IRF used this model to create an STL model from it. But before we go deeper into the simulation, let us discuss the the two models first.

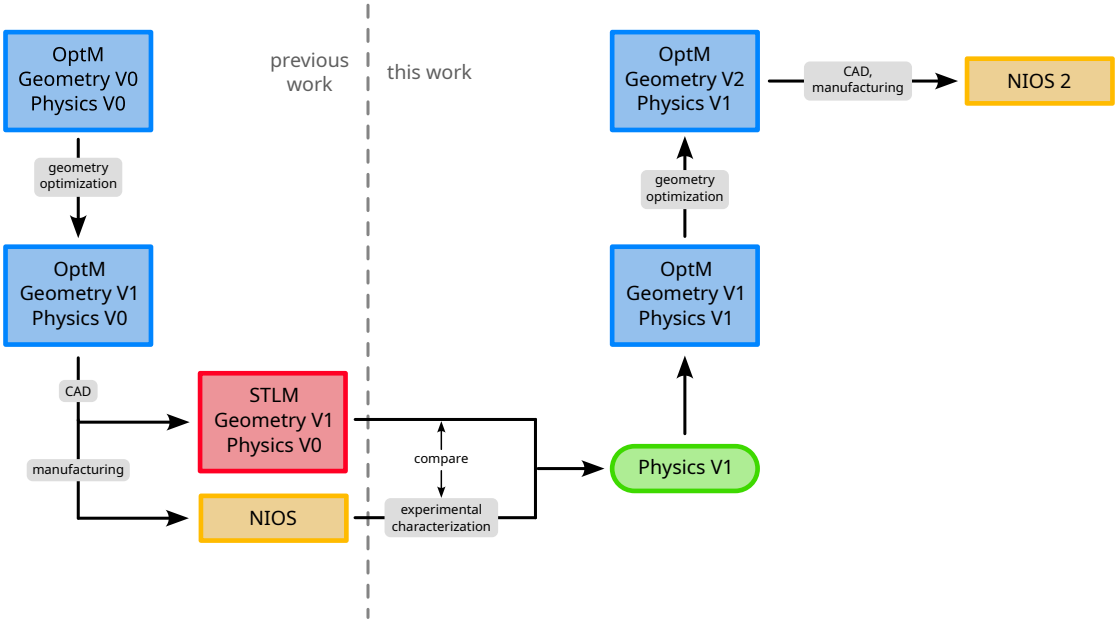

Figure 3.3: Flow chart showing development steps of NIOS with focus on simulation. Blue blocks represent the SIMION optimization models, red the SIMION STL model. "Geometry Vx" describes the version of the geometry and "Physics Vx" the version of the physics that have been implemented in the simulation. Yellow blocks show the physical NIOS. The thesis work starts at the dashed line and entails the blocks right of it with the exception of the CAD and manufacturing part.

3.3.1 Optimization Model

The first optimization model is the result of the previous optimization briefly described in section 3.1. It is defined in a geometry file (`.gem`), native to SIMION. The file contains the instructions on how to set up the different potential arrays. For that, we use a 3D solid geometry modeling language via a series of fill (and other) instructions. In the geometry file we define the simulation volume, symmetries, type (electrostatic or magnetic), and which locations are non-electrode or electrode. This `.gem` file is easy to modify with an arbitrary text editor or with an automated script, since it contains only human-readable ASCII text instructions. The optimization model of NIOS is shown in Figure 3.4 as blue blocks.

The model is symmetric in z, meaning it can be defined in the two-dimensional x-y plane (see Figure 3.2). In both directions z and $-z$ it is infinitely extrapolated. The main use case for the optimization model is to serve as the parameterized object, which is changed for individual optimization steps.

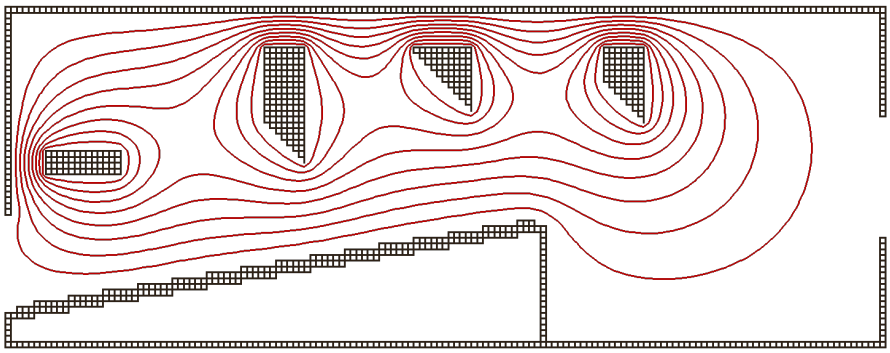

Figure 3.4: Cross-section of NIOS optimization model. Dimension correspond to the original NIOS. Red lines represent equi-potential lines of electric field created by the four electrodes. Particles enter from the left, hit the scattering surface and exit to the right. Black squares show individual potential array points. The scaling factor is 1 mm/gu.

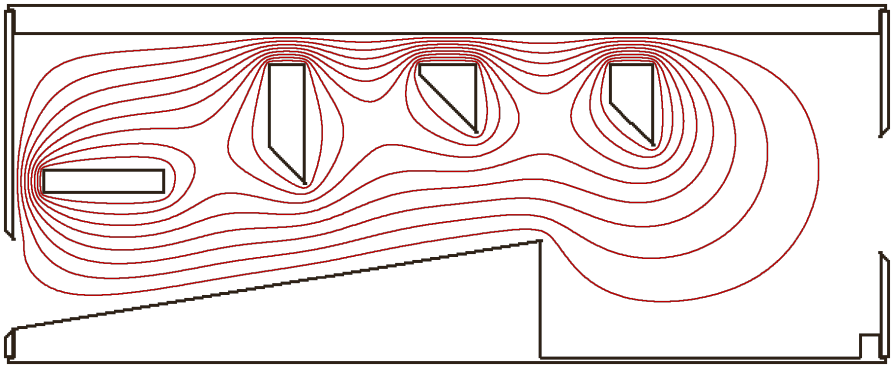

Figure 3.5: Cross-section of NIOS STL model. Red lines represent equi-potential lines of electric field created by the four electrodes. Particles enter from the left, hit the scattering surface and exit to the right. The scaling factor is 0.25 mm/gu.

3.3.2 STL Model

From the optimization model a three-dimensional CAD model was created in order to manufacture NIOS. The CAD model has the file type `.stl` (stereolithography). The `.stl` file can in turn be imported into SIMION to create new potential arrays which accurately represent the real manufactured NIOS geometry. The imported STL model is shown in Figure 3.5. This file cannot be manipulated easily, since it originates from a CAD model.

We use the STL model (in SIMION) to compare the simulated ions with the actually measured ones during the characterization. To be more concrete, what is being compared is the spatial scan from the Faraday cup with a simulated spatial scan in SIMION. Both width and position of the ion peak need to align with the measurements as good as possible.

3.4 Simulation Implementation

In order for the simulation of NIOS to be meaningful, certain interaction mechanisms need to be implemented. By default SIMION comes with the ability to calculate forces acting on charged particles resulting from the potential arrays. Also, particles interact with the geometry in the sense that the particles are terminated upon collision with electrodes or when leaving the simulation volume. SIMION uses an internal flag for the ion's status which is called `ion_splat`. For `ion_splat = 0` the ion is considered to be flying and for `ion_splat != 0` not flying, e.g. splat into an electrode.

Everything necessary for the simulation of NIOS that goes beyond that must be implemented manually by the use of a so called user program. A user program is a script written in the programming language Lua, which allows for extensive customizability of the SIMION simulation.

3.4.1 Implemented Physics

The following physical phenomena are implemented in the simulation:

1. Scattering
2. Charge conversion
3. Molecule dissociation
4. Secondary electron emission
5. Earth's magnetic field

Scattering

When particles from the primary beam, consisting of positive ions, enter NIOS and hit the scattering surface, the particles change their trajectory and their energy.

To first order, the trajectory is reflected according to Snell's law, meaning incidence angle is equal to angle of reflection (Figure 3.6). To second order, the angle of reflection follows a two-dimensional Gaussian distribution. In azimuth direction (yellow surface) the Gaussian is unrestricted, centered at the reflected angle and has a width of $\sigma = 8.5\,\mathrm{mm}$. In elevation (gray surface) the Gaussian has a cut-off, enforced by the scattering surface. It is also centered at the reflected angle and has a width of $\sigma = 6.4\,\mathrm{mm}$. This is motivated by Wieser et al. (2002).

Upon scattering, the projectiles lose part of their energy to the surface. The energy-distribution function for the available experimental setup is not precisely known. We therefore "guess" a reasonable function and adjust it according to the characterization results. An appropriate description of the energy distribution should have a cut-off at the incident energy. It should peak at some point and have a tail towards low energies. This

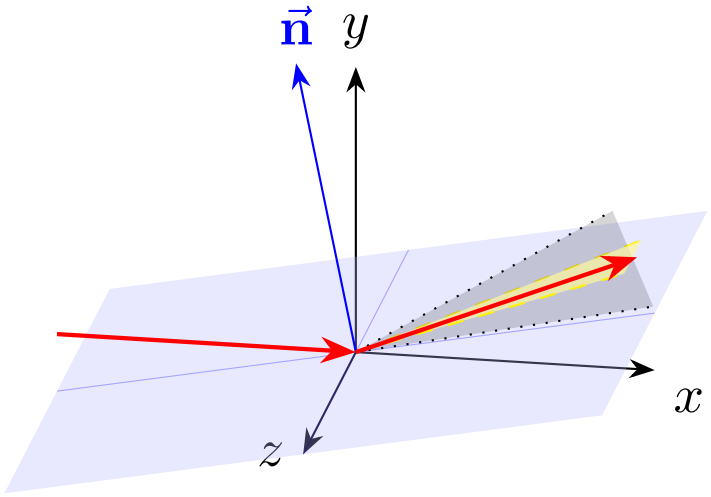

Figure 3.6: Illustration of scattering geometry. With initial direction along the x-axis, the primary ions (red arrow) hit the scattering surface (light blue, with normal vector $\vec{\mathbf{n}}$) and are reflected. The spread of outgoing particles in azimuth is indicated by the yellow surface and in elevation by the gray surface.

is motivated by L'Hoir (1984). A model that fulfills these requirements is an exponentially modified Gaussian distribution

$$f_{\text{energy}}(x) = \frac{A}{2\eta}\, e^{\frac{\sigma^2}{2\eta^2}}\, e^{\frac{x-\overline{x_g}}{\eta}} \left[1 + \operatorname{erf}\left(\frac{1}{\sqrt{2}}\left(\frac{\overline{x_g}-x}{\sigma} - \frac{\sigma}{\eta}\right)\right)\right], \tag{3.16}$$

with A being the enclosed area, $\overline{x_g}$ and σ the mean and width of the Gaussian part, and η the width of the exponential part. The function is taken from Wieser (2001). The distribution used for the simulation is depicted in Figure 3.7 for $\overline{x_g} = 0.95$, $\sigma = 0.02$ and $\eta = 0.3$. A is scaled in such a way that the maximum value of f_{energy} is 1. Scattering is only implemented at the scattering surface.

Charge conversion

When ions from the primary beam scatter, they undergo charge exchange. They leave the scattering event in one of three charge states – neutralized, positively ionized or negatively ionized. Each state has a probability, which is not precisely known. In the simulation each incident ion creates one particle of each charge state, so three scattered particles per incident particle. We can account for different yield rates during data analysis by scaling the count rates accordingly. This approach has a computational advantage. Assume 5 % of the incident ions are converted into negative ions during a simulation run. We would have to start the simulation with 20 times more particles to get the same amount of negative ions compared to a run with 100 % conversion efficiency and then scaling the count rates later.

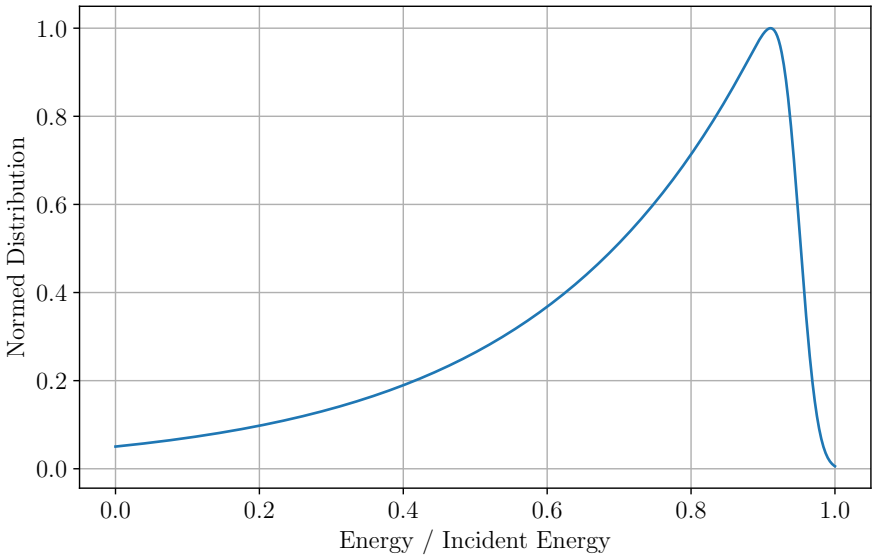

Figure 3.7: Energy-distribution function of scattered particles in units of and relative to incident energy. The function follows an exponentially modified Gaussian.

Molecule dissociation

During both the calibration of NILS and consequently the characterization of NIOS the main interest were hydrogen ions. Because the beam intensity for atomic H^+ is relatively small, the measurements were done with molecular H_2^+. When molecules scatter, they have a probability to dissociate, meaning the atoms are no longer bound to each other and travel individually. The probability is dependent on their kinetic energy. Measurements from NILS have shown that for the energy range used in the NIOS characterization basically all molecules dissociate into atomic hydrogen. Therefore, in the simulation the dissociation probability is 100 %. When molecular H_2^+ dissociates, the remaining energy after the scattering event is shared approximately equally among the individual atoms. Approximately, because the energy depends on the direction the atoms dissociate into. In the extreme case the dissociation axis is aligned with the travel direction, giving one of the atoms more and the other one less than 50 % of the energy (disregarding the energy-loss from scattering). This effect, however, is negligible and not implemented in the simulation.

Secondary electron emission

When any particle hits a surface, there is a chance to create secondary electron emission. The electrons have an energy of approximately 2 eV and are ejected in a random direction. The electron yield is set to be 1. For the simulation it does not matter whether the yield is higher or lower. It is only interesting to evaluate the electron trajectories, which is independent of the yield.

Earth's magnetic field

Especially for the secondary electrons the magnetic field of the Earth cannot be neglected and needs to be implemented. An typical measurement of the magnetometer of IRF (Yamauchi et al., 2024), which is located close to the calibration facility, shows approximately

$$\mathbf{B}_{\text{earth}} = (10500, 200, 52200)\,\text{nT}. \tag{3.17}$$

B_x points horizontal northward (geographical), B_y horizontal eastward and B_z vertical downward. We know the orientation of NIOS in relation to this coordinate system and can therefore transform $\mathbf{B}_{\text{earth}}$ into the coordinate system of the simulation.

3.4.2 Technical Implementation

The physical phenomena described in subsection 3.4.1 need to be implemented in a Lua-script. In SIMION this file is called user program and it has a distinct structure. It can consist of multiple program segments, each with its specific purpose and specific read/write access to reserved variables. Reserved variables always start with the prefix `ion_` and can only be accessed during certain stages of the user program. We use the segments

1. `segment.flym`
   Starting a simulation is called `Fly'm`. The program segment `segment.flym` is executed at the start of a such a `Fly'm`. It loads the geometry from the geometry file and starts the simulation with the `run()` command, which does an entire particle tracing run.

2. `segment.init_p_values`
   At the beginning of a run, before any particles are flown, this program segment adjusts the electric potential arrays. Here we can define the voltage of the electrodes of NIOS.

3. `segment.initialize`
   This program segment is called each time a particle is initialized. It has access to ion properties and is used to write initial values into a log file.

4. `segment.mfield_adjust`
   This segment can be used to examine and change the magnetic field for each time step. Since the Earth's magnetic field is considered to be constant for the simulation, the field only needs to be set, not changed. The segment therefore sets the magnetic field at the location of the ion to $\mathbf{B}_{\text{earth}}$, as stated in Equation 3.17.

5. `segment.other_actions`
   After every time step `segment.other_actions` is called. It is used to manipulate ion parameters, e.g., mass, velocity, splat, etc. The change of these parameters is determined by the implemented scattering, charge conversion, molecular dissociation and secondary electron emission. Another function in this segment logs certain

Table 3.1: Ion properties set at the start of a simulation run.

Property	Value
Mass [u]	`ion_mass` = 2.014552933624
Charge [e]	`ion_charge` = 1
Color	`ion_color` = 1 (red)
Location [mm]	`ion_px_mm, ion_py_mm, ion_pz_mm`
Velocity [mm/µs]	`ion_vx_mm, ion_vy_mm, ion_vz_mm`
Kinetic Energy [eV]	integrated in velocity

events, such as splats. That is important for analyzing the performance of NIOS afterwards.

6. `segment.terminate`
   This segment is called after all ions have died. It is used to close the log file and output information about the run.

Let us now illustrate one simulation run by explaining the different paths a particle can take. First we load the geometry and set the voltage for the NIOS electrodes. Then a particle is initialized outside of NIOS in front of the entrance with the properties shown in Table 3.1. We fly a H_2^+ particle, which is represented by a mass of two proton masses and a charge of 1. The ion color is useful for book keeping. It allows us to differentiate between a positive primary ion and a positive scattered ion. The initial location follows a uniform circle distribution. The ion can be initiated anywhere within this circle with equal probability. The circle is large enough to cover the entrance of NIOS. The velocity is defined by direction and kinetic energy. The direction follows a uniform cone distribution with the axis parallel to the x-direction. The ion therefore enters NIOS in the same way as the ions do in the experiment.

Now the simulation run starts. One time step passes. The particle moves according to its velocity towards the entrance of NIOS. For each time step, SIMION calculates the forces acting on the ion due to the electric and magnetic potentials. The forces result in a change of velocity. At the end of the current time step, `segment.other_actions` is called. Here we implemented a scatter query. Did the ion splat? If no, it can continue flying. If yes, it has either left the simulation volume and is not of interest anymore or it splatted on a surface. In case the surface is not the scattering surface, only a secondary electron is produced.

The secondary electron is set to have a kinetic energy of 2 eV. The direction follows a uniform spherical distribution, meaning it can point in any direction with equal probability. This leads to the problem, though, that half of the produced electrons immediately hit the surface again from which they came. We therefore produce two electrons with opposing velocity directions. One

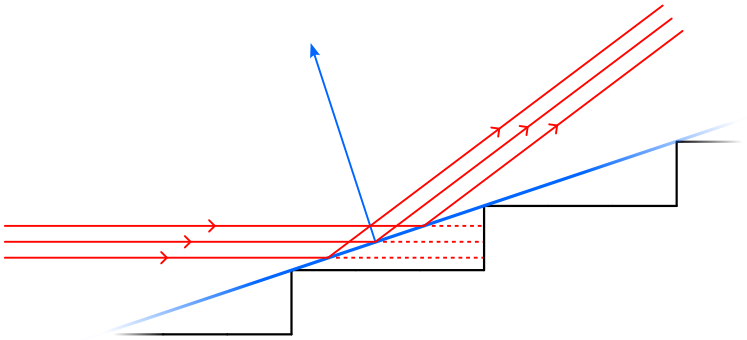

Figure 3.8: Illustration of backtracing. Ions (red) splat on the pixelated scattering surface (black). Their intersection with the ideal scattering surface (blue) is calculated and the ions are relocated onto the intersection point. From there, the regular scattering continues.

electron flies away from and the other one into the surface. The rare case of the velocity vector being parallel to the surface can be neglected. Both electrons are flown, one after the other, until both have died by splatting or leaving the simulation volume.

If the primary ion indeed hit the scattering surface, not only a secondary electron is created, but also scattering takes place.

When a primary ion is registered to have splat on the scattering surface, first of all, it is slightly backtraced. The reason for that is illustrated in Figure 3.8. The electrode points in the simulation have a discrete size. If we take a closer look at the scattering surface, it seems to be "pixelated" and we get unwanted scattering behavior from that. The ion can get stuck on one of the steps of the staircase. Therefore we backtrace the ion. We find the intersection of the ion's trajectory with the ideal scattering surface and place the ion at the intersection. The new scattered direction follows a two-dimensional Gaussian distribution, centered at the specular reflection, as discussed in subsection 3.4.1. When the ion scatters we create three new particles, one for each charge state. All three new particles have half of the mass of the incident ion, due to the molecule dissociation. The new energy is halved as well. Up to this point, we have not taken energy-loss into account. The new energy needs to be adjusted to follow the distribution shown in Figure 3.7. Now it becomes handy that the distribution is normalized such that the maximum is 1. We simply draw a random point (p_x, p_y) with $p_x, p_y \in [0, 1]$. If the point lies above the graph, we draw again. If the point is below the graph, we multiply the halved incident energy by p_x.

All three new particles continue flying, one after the other. For each time step the

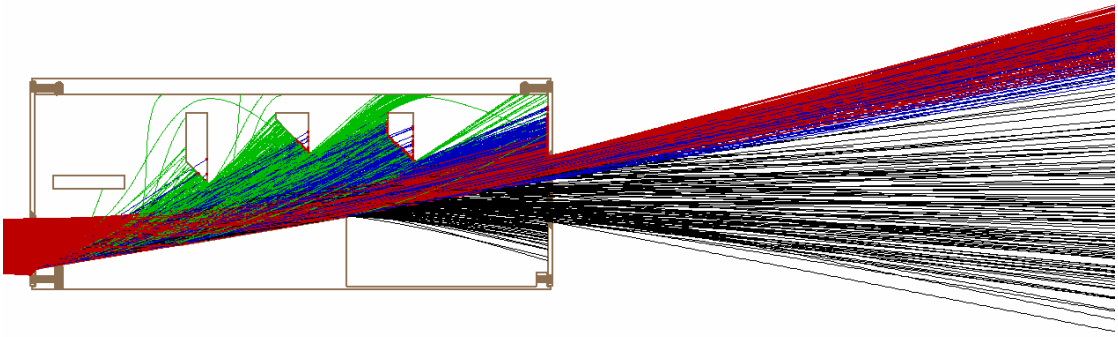

Figure 3.9: Simulation of STL-model. Primary beam ions (red) enter from the left. Scattering products are negative ions (black), positive ions (green), and neutrals (blue). Secondary electrons are not shown. Primary beam energy is 1300 eV. 10000 initial particles.

forces acting on them are re-evaluated and the velocity changed accordingly. The simulation carries on until all three particles have died by either splatting (and creating secondary electrons) inside of NIOS or by leaving it. If they manage to leave NIOS, they can be detected by a detection plane. The plane sits at a distance to the NIOS exit, which represents the distance between NIOS and Faraday cup in the experimental setup (≈ 300 mm). When particles reach the detection plane, they are logged with their properties (mass, charge, position, velocity, energy, etc.) at the time of the detection.

The above paragraphs describe the simulation of a single particle. The process is repeated for as many particles as we want.

3.5 Analyzing a Simulation Run

So far we have managed to simulate the desired behavior of NIOS. The incoming ions scatter and produce different particle populations, which are detected at the detection plane. Now we need a way to compare the performance of different simulation runs with each other.

Before we dive into quantitative methods, we can visually inspect the particle trajectories depicted in Figure 3.9. Seeing this, we should not be surprised anymore about a high positive ion flux at the far end of the spatial scan (which was discovered during the early characterization, when the range of the spatial scan was considerable larger). Due to the electric field created by the electrodes, the primary ion trajectories (red) are bend away from the scattering surface, so they move through NIOS unhindered. We can also see neutrals (blue) finding a way out.

The visual inspection is useful to get a rough idea about what is going on inside NIOS, but we want to actually compare the simulated output with the characterization results. The detection plane acts similar to the Faraday cup and the log file can be seen as a measurement with some remarks. Since there is no actual spatial scan performed, the

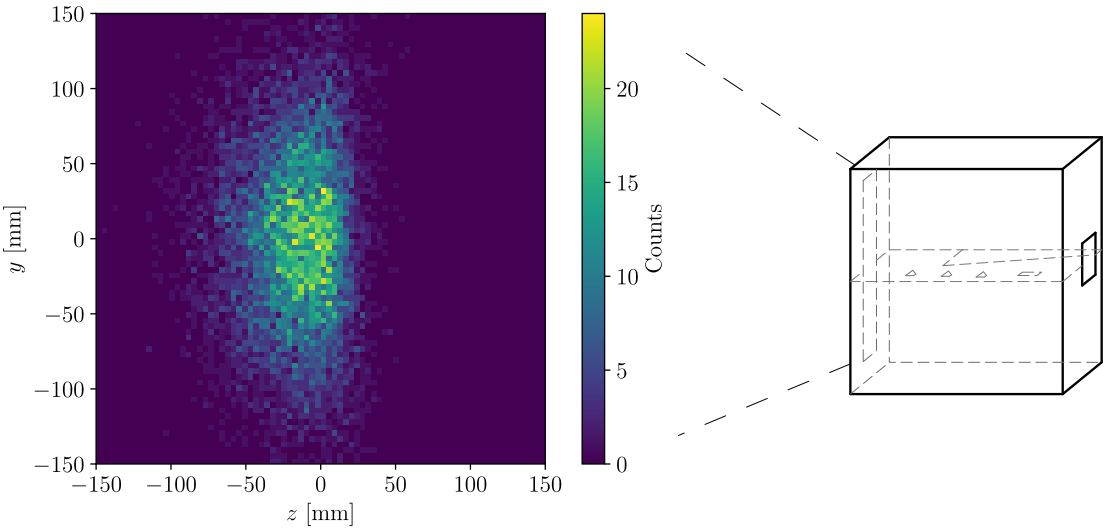

Figure 3.10: 2D-histogram showing negative ion counts at the detection plane. The primary ion beam energy is 1300 eV. The z-axis corresponds to the z-axis of the spatial scans during the experimental characterization. 100 000 primary particles are flown.

data is not convoluted with any function. Also, what the log file provides are counts, not a current. We can create a two-dimensional histogram from it, showing the counts in relation to their position. Figure 3.10 shows an example 2D-histogram.

In order to make it comparable to a spatial scan from the characterization, we need to collapse the 2D-histogram in one dimension. It is important to pick the correct dimension such that the remaining dimension corresponds to the z-axis from our spatial scans. We then get a 1D-histogram along the same axis as the scan. Since the two coordinate systems – simulation and vacuum chamber – do not have the same origin, the histogram needs to be shifted such that the origins along this axis do align. An example 1D-histogram, in the following called simulated scan, can be seen in Figure 3.11.

We perform a Gauss fit to have a measure for the location of the ion peak. The simulated scan is now in a state that can be compared to the real deconvoluted z-scans. The choice of a Gaussian fit function is motivated by the characterization results.

3.6 Adjusting the Simulation with Characterization Results

What does “adjusting the simulation” mean exactly and which are the parameters that can be adjusted? To answer these questions, we compare a real scan with its corresponding simulated scan and see that both show an ion population. In the case of the real scan it takes the form of a Gaussian shaped dip, since it is a current density with a negative sign. For the simulated scan it is a Gaussian shaped peak, since it shows counts. The amplitude of both Gaussians cannot be compared without further processing. What is more important than the amplitude, is the location of the extrema. The location of them

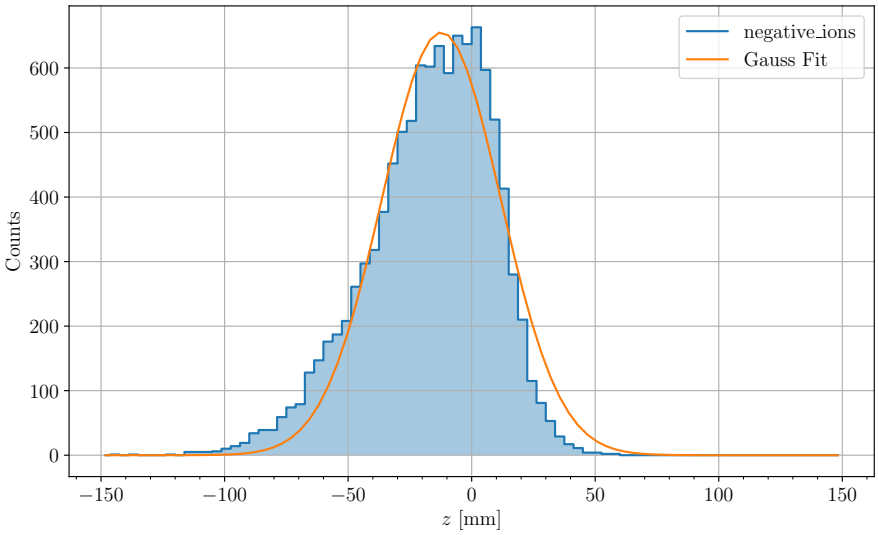

Figure 3.11: 1D-histogram showing negative ion counts over the z-axis. The Gauss fit is used to find the center and width of the distribution. The primary ion beam energy is 1300 eV. 100 000 primary particles are flown.

can be compared and that is precisely what we do.

We need to find ways to move the location of the ion peak in our simulated scans. Possible parameters to tinker with are the dissociation rate, the energy-distribution function and the potential of the NIOS electrodes. The latter changes the trajectory of the charged particles, which shifts the beam center. It is not a suitable candidate, however, because during the real measurements the potential was always dependent on the incident beam energy. Therefore it should stay that way for the simulated scans. The dissociation rate changes the shape of the peak, because – assume the rate is 50 % – two peaks will start to appear, one for the dissociated atoms and one for the molecule. The molecule has about double the energy of the atoms and is therefore less prone to change its trajectory due to the Lorentz force than the less energetic atoms. The analysis of NILS data, which can resolve energy, showed no trace of the molecule population. We assume therefore a dissociation rate of practically 100 %. What remains is the energy-distribution function (Equation 3.16). Changing the shape of the function has a similar effect as changing the electrode potential. The lower the energy, the more the ion trajectory changes in the electric field. Since the initial shape of the function was only estimated, it makes sense to adjust it such that the result resembles our measurements better.

We adjust the energy-distribution function for the energy 1300 eV. The real distribution function is dependent on the incident energy and the exact angle of incidence. For this work the energy-distribution function is simplified and not energy dependent. This is an aspect for a potential continuation of the project.

Table 3.2: Comparison of ion extrema between simulation and characterization for different primary beam energies. z_0 and σ describe the center and standard deviation of the fitted Gauss function. Quantities are denoted by $_{\text{char}}$ when coming from the characterization and $_{\text{sim}}$ when coming from the simulation.

Energy [eV]	$z_{0,\text{sim}}$ [mm]	$z_{0,\text{char}}$ [mm]	σ_{sim} [mm]	σ_{char} [mm]
5000	-10.5 ± 0.6	-15.2 ± 1.7	24.1 ± 0.6	21.1 ± 2.4
3000	-9.6 ± 0.6	-15.5 ± 3.0	23.8 ± 0.6	26.7 ± 4.2
2000	-9.1 ± 0.7	-13.4 ± 2.9	24.0 ± 0.7	24.7 ± 4.3
1300	-9.3 ± 0.7	-10.5 ± 1.7	23.9 ± 0.7	25.0 ± 2.6
900	-9.3 ± 0.7	-5.7 ± 1.7	24.5 ± 0.6	19.9 ± 2.7
600	-9.2 ± 0.7	-1.2 ± 1.5	24.4 ± 0.7	20.8 ± 2.0
450	-9.0 ± 0.7	0.5 ± 0.8	24.9 ± 0.7	21.0 ± 1.0

3.7 Simulation Results and Discussion

Let us remind ourselves of the goal of this simulation chapter. The goal is to implement a simulation, which is first applied to the NIOS STL-model. We want to compare the simulated scans with the real ones and adjust the user program such that the simulated scans resemble the real ones. In the picture of Figure 3.3 we have then reached the green block *Physics V1*.

We run the simulation for all seven different energies used in the characterization and determine the Gauss parameters (z_0 and σ) for the ion peak. The Gauss parameters from the simulation and from the characterization are shown in Table 3.2. We decided for the simplified non-energy dependent energy-distribution function. This means that some energies will be represented better than others. We adjust the energy-distribution function such that the ion peak is centered at around $-10\,\text{mm}$ and has a standard deviation of around $24\,\text{mm}$. The energy-distribution function that leads to this shape and location of the ion peak is defined by Equation 3.16 with the parameters $\overline{x_g} = 0.95$, $\sigma = 0.02$ and $\eta = 0.3$. A is scaled such that the maximum value of f_{energy} is 1, as described earlier.

Table 3.2 shows us how well the simulation and the characterization match. In general, for all energies the match can be described as good. Since the simulation is energy independent the location of the peak does not change a lot for the different incident beams. The location average is at $-9.4\,\text{mm}$. The differences between the peak location of the simulation and the characterization range from $-1.2\,\text{mm}$ to $9.5\,\text{mm}$. The match is best for the $1300\,\text{eV}$ beam and worst for $450\,\text{eV}$. When looking at σ_{char}, we see that for the characterization the values lie in the interval from $19.9\,\text{mm}$ to $26.7\,\text{mm}$. The σ_{sim} values resulting from the simulations all lie in this interval, with an average of $24.2\,\text{mm}$. We can conclude that, in general, the simulation matches the characterization well. It matches especially well for the $1300\,\text{eV}$ beam. If one wants to improve the match also for the other energies, a energy-dependent energy distribution function is necessary.

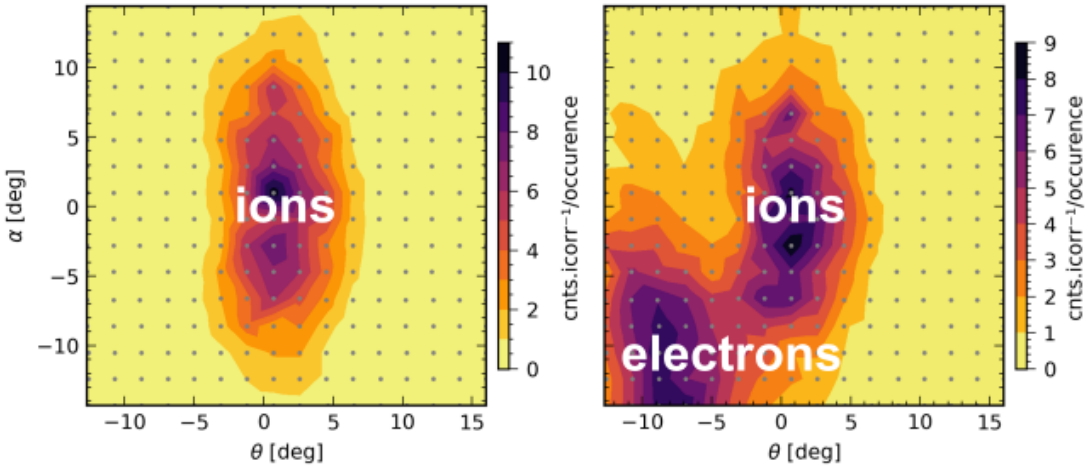

Figure 3.12: Angular response of NILS, x- and y- axis show different directions. The coordinate origin points towards NIOS. *Left:* NILS' magnet is switched on, which prevents electrons from entering. *Right:* NILS' magnet is switched off. Electrons can enter. Credit: Romain Canu-Blot, personal communication.

Compared to *Physics V0*, we have achieved major improvements by implementing the physical concepts introduced in subsection 3.4.1: Scattering, charge conversion, molecular dissociation, secondary electrons and Earth's magnetic field. It is important to note that the possibility to simulate secondary electrons was mainly used to investigate the floor population. We tried to find an answer to the question: How do electrons travel from the NIOS electrodes to the detector? Measurements done by NILS show an electron population with an energy that corresponds to the NIOS electrode voltage. These "NIOS electrons" can be seen in Figure 3.12. The plots depict the angular response of NILS. x- and y- axis are two spherical coordinates with the origin pointing towards NIOS (compare with the experimental setup in Figure 2.3 and exchange the Faraday cup with NILS). The two panels show two different measurement modes. In the left panel a magnet is switched on. The magnetic field blocks electrons from entering NILS. Only the expected negative ion population is visible, coming from the direction where NIOS sits. In the right panel the magnet is off and electrons can enter. The measured population enters NILS from an unexpected direction. The majority of these NIOS electrons has an energy that corresponds to the NIOS voltage. These electrons must therefore originate at the electrodes. The simulation of secondary electron emission could not explain how the electrons reach the detector.

In Figure 3.13 we can see the simulated trajectories of secondary electrons in orange. There are no electrons which originate from the electrodes and manage to leave NIOS. Only some electrons, created at the edge of the exit aperture, can be seen gyrating outside. Their gyroradius is about 10 cm, which corresponds to a kinetic energy of about 3 eV. This is to be expected for secondary electrons that are only minimally accelerated by the stray electric field from the electrodes outside of NIOS.

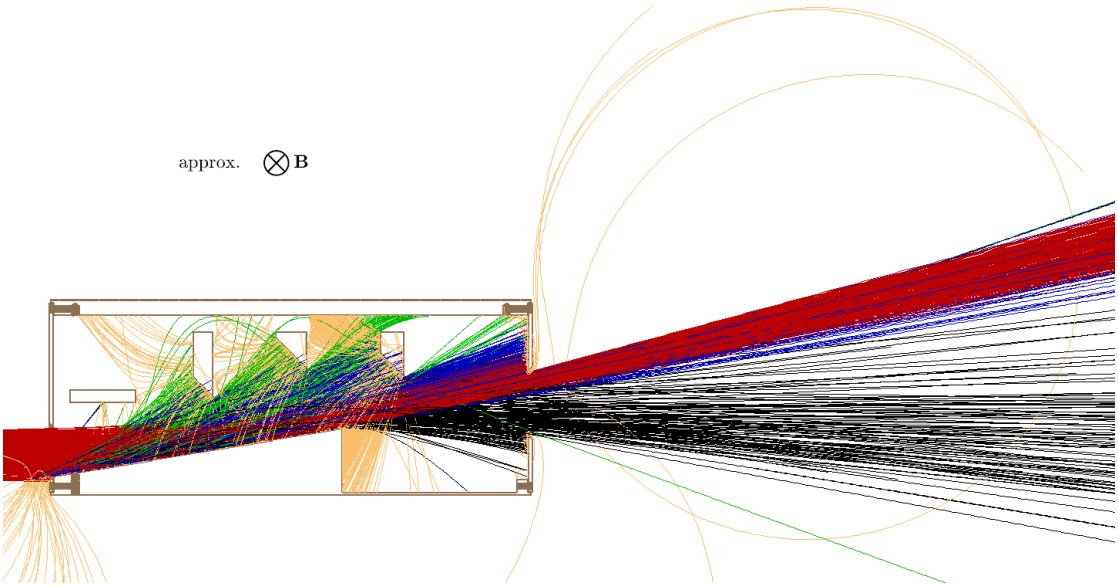

Figure 3.13: Simulation of STL model with secondary electron emission. The primary ions are drawn in red, scattered positive ions in green, scattered neutrals in blue, scattered negative ions in black and secondary electrons in orange. The approximate direction of Earth's magnetic field points into the figure plane.

So what is missing? The most likely reason is an incomplete simulation. In the current implementation, only the primary ions can scatter exactly once and only on the scattering surface. In reality multiple scattering exists for atoms, ions and secondary electrons. For the multiple scattering hypothesis of electrons speaks the energy spectrum measured by NILS. In the spectrum there is a peak at the energy that corresponds to the NIOS voltage and a tail towards low energies. Most electrons scatter fully elastic, creating the peak. Some electrons, however, lose some energy upon scattering, creating the tail towards low energies. Multiple scattering opens up many new ways for more complex trajectories. We demonstrate one possible path with multiple scattering in Figure 3.14 by placing (initiating) particles manually at certain locations. The electrons are initiated with 2 eV at the backside of the right-most electrode (orange trajectories). In the simulation, this surface is not illuminated by particles. In reality, e.g., the neutral atoms from the main scattering surface can scatter multiple times at the inside surfaces of NIOS such that they reach the backside of the electrode. The secondary electrons created at the electrode are accelerated and can hit the edge of the exit aperture. At the edge they have approximately the energy corresponding to the NIOS voltage. The electrons scatter (mostly fully elastic, no energy loss) at the edge and can then reach NILS (red trajectories). NILS sees the electrons coming from a different direction than the ions, because of the bend trajectory. This demonstrated process is not unique. One can think of other trajectories based on multiple scattering that lead to such trajectories.

We can conclude that the simulation lacks multiple scattering to explain the electrons

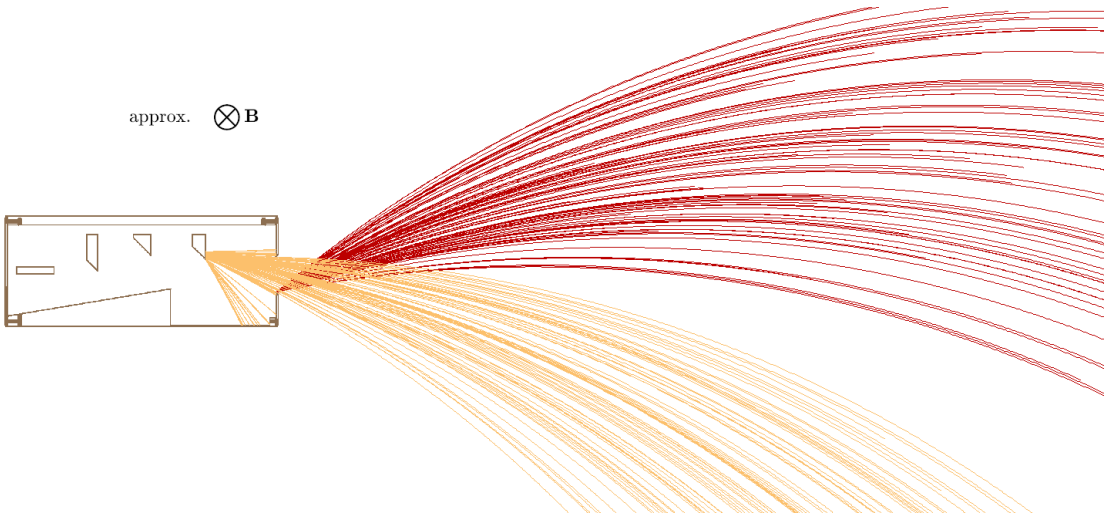

Figure 3.14: Demonstration of multiple scattering. Both colors represent electron trajectories. Electrons (orange) manually initiated at the right-most electrode can hit the edge of the exit aperture. There they can scatter and follow trajectories (red) that potentially reach NILS.

seen by NILS. But is it worth implementing this process? The short answer is no. We would not gain information about the electron flux, because there are too many unknown variables. To be able to give statements about the flux, we need to know the precise scattering efficiency for primary ions and for scattered neutrals and scattered ions, as well as precise secondary ion yields. Apart from the electron flux, we could gain information about the electron trajectories. But since we already know that the electrons *must* be created at the electrodes (because of their energy), we can skip finding the exact paths, which lead to their creation. Instead, we can directly initiate electrons with the appropriate energy at the exit of NIOS with lots of different velocity directions and see which trajectory leads to NILS.

Since for NIOS negative ions are the main particle species of interest and not electrons, we set the secondary electron yield to zero for the following simulations and in particular the optimization. Remember that the improvement of the simulation above was done by using the NIOS STL-model. It resembles the physical NIOS and was therefore the best choice for this task. In the next section, the optimization, we repeatedly want to change the geometry to increase the performance of NIOS. The STL model is not appropriate for that, because it cannot simply be changed. This is why we apply our findings – which we used to create the improved SIMION user program – to the optimization model. As discussed earlier, this model defines the geometry with a `.gem` file, where variables can be declared and changed easily. So both STL and optimization model now make use of the improved implemented physics.

4 Optimization

The improved simulation lays the foundation for the third and final task of this work: developing an improved version of NIOS. We do this by parameterizing the geometry and applying an algorithm that finds the best values for the parameters.

4.1 Optimization Objectives

During the characterization and simulation of NIOS, we have identified the following problems, which are to be improved:

- A substantial amount of primary ions exit NIOS without surface interaction. The simulation has revealed that they are bent away from the scattering surface by the electric field from the NIOS inner electrode. These ions fly right through NIOS and do not produce any negative ions. Measured with the Faraday cup, this population results in a current 100-times larger than the current produced by the negative ions. If measured with a more delicate instrument, this sudden increase can lead to severe saturation of the instrument. We therefore want to inhibit any primary ions from leaving NIOS without surface interaction.
- Fewer primary ions hitting the scattering surface means fewer charge conversions and fewer negative ions. We therefore want to maximize the amount of primary ions hitting the scattering surface. This fraction of particles differs from the previously mentioned one in the sense that there can be primary particles that do not hit the scattering surface, but remain inside of NIOS.
- We want to minimize the amount of unwanted scattered particles leaving NIOS. These are the positive ions and neutral atoms after the scattering process.
- In general, we want to maximize the negative ion yield of NIOS.

In addition to these problems, we have identified two requirements, which were previously not violated and have to remain that way.

- The total volume of NIOS is restricted by the available space inside the calibration tank and can therefore not be larger than these limits.
- We want the output beam to have a bulk velocity vector that is as parallel as possible to the primary beam axis. This makes future experimental setups easier, because we do not have to position instruments or NIOS in inconveniently angled ways.

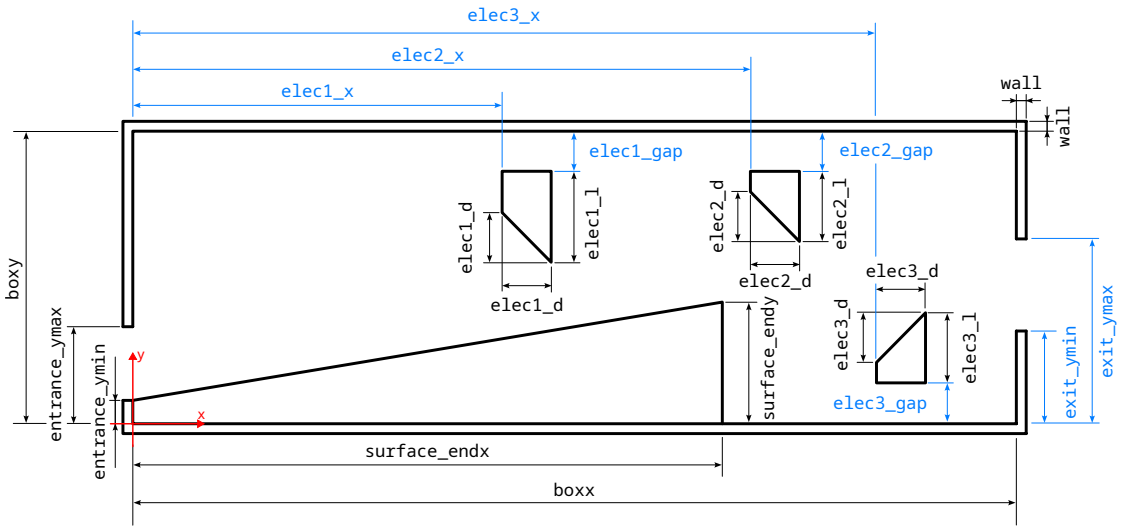

Figure 4.1: Parameterization of new NIOS optimization model. Black measurements are fixed and blue ones are to be optimized. The figure is not to scale.

4.2 Optimization Setup and Parameters

To perform the optimization we need three ingredients, which fully describe what we want to optimize and how we want to optimize. Their full definition is given in the following subsections.

1. A solution to the optimization problem, which consists of a set of parameters,
2. a way to evaluate the "goodness" or "fitness" of the solution,
3. and an algorithm that probes the parameter space in search for the best solution.

4.2.1 Definition of a Solution

An individual solution is defined as one unique set of parameters that fully characterizes the geometry of NIOS and the voltage of the NIOS electrodes. The geometry parameters are defined in the `.gem` file of the optimization model (compare with Figure 3.3 to see the two different types of models). In the `.gem` file we define the geometry via various fill (and other) commands. For example, a command like `fill{within{box(x1,y1,x2,y2)}}` creates a solid rectangular electrode that stretches from the point (x_1, y_1) to the point (x_2, y_2). With these commands we can fully parameterize the NIOS geometry. The different parameters and their relation to each other are shown in Figure 4.1.

There are parameters, which are confined by other means, e.g., the total volume of NIOS is limited by the space on the translation table. These parameters are drawn in black in the figure. The length, width and height are therefore fixed and not subject to the optimization. The position and size of the entrance are chosen to stay as they are. That way, the new NIOS can be positioned in the calibration chamber exactly like the old one, having to adjust neither hard- nor software. Parameters, which are free and need to

Table 4.1: Table showing parameters defining NIOS. The parameter names are defined in Figure 4.1.

Parameter	Type
`wall`	fixed
`boxx`	fixed
`boxy`	fixed
`entrance_ymin`	fixed
`entrance_ymax`	fixed
`surface_endx`	fixed
`surface_endy`	fixed
`elec1_l`	fixed
`elec1_d`	fixed
`elec2_l`	fixed
`elec2_d`	fixed
`elec3_l`	fixed
`elec3_d`	fixed
`exit_ymin`	free
`exit_ymax`	free
`elec1_x`	free
`elec1_gap`	free
`elec2_x`	free
`elec2_gap`	free
`elec3_x`	free
`elec3_gap`	free
`voltage`	free

be optimized, are shown in blue. During trial optimizations the shape of the electrodes was determined. For the final optimization only the location (`elecX_x`, `elecX_gap`) is to be optimized. A full list of free and fixed parameters that define NIOS is given in Table 4.1. To the geometry-defining set of free parameters above, we add the potential of the electrodes. That gives us our full set of 9 parameters that are to be optimized.

4.2.2 Fitness of a Solution

In order to compare different solutions with each other, i.e., different sets of values for the free parameters, we need to define the fitness of a solution. The most important aspect is the number of negative ions n_{neg} reaching the detection plane. We therefore count them in the log file. We do the same with the other two scattering products, the positive ions and the neutrals, and get n_{pos} and n_{neut}. For the negative ions only, we evaluate the bulk parallelity P to the x-axis (compare Figure 4.1).

For each negative ion, we take the velocity vector $\mathbf{v}_i$ and normalize it to get

$\hat{\mathbf{v}}_i$. We then define the individual parallelity P_i as

$$P_i = (\hat{\mathbf{v}}_i \cdot \hat{\mathbf{x}})^4, \tag{4.1}$$

with $\hat{\mathbf{x}}$ being the unit vector in the x-direction. We raise the scalar product to the power of 4 in order to make it more sensitive to small changes. The bulk parallelity is then the mean of all individual parallelities

$$P = \sum_i^n \frac{P_i}{n}. \tag{4.2}$$

P will be in the interval [0,1], with 1 meaning the bulk velocity is exactly parallel to the x-axis and 0 meaning it is perpendicular to x.

Apart from evaluating the particles that reach the detection plane, there are two more criteria, which influence the fitness. First, if any primary ions reach the detection plane, the fitness is penalized and set to the worst possible value. We want to avoid any solutions that allow this behavior. Then, we take into account the amount of primary ions that die inside NIOS without hitting the scattering surface. This amount is denoted as n_{unscat}, for unscattered.

Now remember that we produce three particles for each scattered primary ion. n_{neg}, n_{pos}, and n_{neut} are therefore too large. We assume that the positive and negative ion population are of approximately the same size and each are about 5 % of all scattered particles (Wieser et al., 2002). This leads to correction factors

$$k_{\text{neg}} = k_{\text{pos}} = 0.05 \tag{4.3}$$

$$k_{\text{neut}} = 0.90. \tag{4.4}$$

We normalize all n_i with the total number of flown primary ions n_{prim}. Last, we combine every n_i with a weight w_i. The weight allows us to adjust the impact and sign of the specific factor. The final fitness function becomes

$$f_{\text{fitness}} = w_{\text{neg}} \frac{k_{\text{neg}}\, n_{\text{neg}}}{n_{\text{prim}}} P + w_{\text{pos}} \frac{k_{\text{pos}}\, n_{\text{pos}}}{n_{\text{prim}}} + w_{\text{neut}} \frac{k_{\text{neut}}\, n_{\text{neut}}}{n_{\text{prim}}} + w_{\text{unscat}} \frac{n_{\text{unscat}}}{n_{\text{prim}}}. \tag{4.5}$$

After the initial guess, the exact choice of the weights follows trial and error. The following weights in Table 4.2 led to good results. All of the weights have a positive sign, which means they increase the fitness (worse), except for w_{neg}. The negative sign means that negative ions decrease the fitness (better).

4.2.3 Genetic Algorithm

Now that we have defined what a solution is and how we can quantify its fitness, we need a way to find the best solution. This is the actual optimization. We chose a member of the group of evolutionary algorithms: the genetic algorithm. Genetic algorithms are

Table 4.2: Weights for different particle populations.

Weight	Value
w_{neg}	-100
w_{pos}	1
w_{neut}	30
w_{unscat}	15

algorithms inspired by nature that make use of the mechanics of natural selection and natural genetics (Goldberg, 1989).

Based on Eiben and Smith (2015) "3.2 Components of Evolutionary Algorithms" (simplified, to prevent this subsection from becoming a biology lecture), we define the building blocks of the genetic algorithm in the following paragraphs. The python module `geneticalgorithm`[1], which is used for this work, provides these building blocks. The key words in italic are the algorithm settings from this module.

Individual Solution and Fitness Function The definitions of the first two points are covered in detail in the previous subsections – an individual solution is one possible geometry of NIOS and the fitness function describes how "good" the solution is. In the context of genetic algorithms, an individual solution is also called a chromosome, because they hold different genes. Genes are the free parameters that are adjusted during the optimization (e.g., `exit_ymin`, `exit_ymax`, etc.).

Population and Generations The population consists of multiple individual solutions and is characterized by the *population size*. Changes to the population lead to new generations of the population. This represents the evolutionary aspect of the algorithm. The *number of generations* dictates for how many iterations the optimization runs. To create the next generation of the population, new individual solutions need to be created.

Parents A parent is an individual solution, which has been selected to undergo a variation to create offspring. The selection probability is proportional to their fitness, meaning fitter solutions are more likely to become parents. This selection method is known as roulette wheel, where a section of the wheel represents an individual and the section is larger the fitter the individual is. If individuals with lower fitness would be completely ignored, the algorithm could get stuck in a local optimum more easily, therefore they still have a small probability to be selected. Not all current individuals become parents, only a *parent portion*.

Crossover and Mutation To create new offspring from two parents, we use crossover. This leads to two children having certain characteristics from both of their parents. The

[1] https://pypi.org/project/geneticalgorithm/

Table 4.3: Genetic algorithm settings.

Parameter	Value
`max_num_iteration`	100
`max_iteration_without_improv`	100
`population_size`	50
`parents_portion`	0.3
`elit_ratio`	0.02
`crossover_probability`	0.7
`crossover_type`	`"uniform"`
`mutation_propability`	0.2

hope is that one child receives all the good characteristics, such that we end up with a child that is fitter than each of its parents. This crossover operation is applied to the offspring with a certain *crossover probability*. The offspring, whether they were subject to crossover or not, mutate with a certain *mutation probability*. That means that a gene (e.g., `exit_min`) is randomized within the set boundaries. This helps to move away from local optima in the parameter space and create completely new solutions.

Elitism Last, because we do not want to lose very good solutions, there is elitism. A certain *elite ratio* of the current population is transferred unchanged to the new generation, usually just a few individuals.

The whole process of generating a new population from the current one is depicted it Figure 4.2. To sum it up, the described algorithm is based on multiple generations of a population that undergo selection (survival of the fittest) and variation (crossover and mutation). With this method we intend to probe the large parameter space effectively and find a suitable new geometry for NIOS.

4.2.4 Optimization Parameters

The genetic algorithm can be adjusted with the settings: maximum number of iterations, maximum iterations without improvement, population size, parent portion, elite ratio, crossover probability, crossover type, and mutation probability. During the course of the optimization, different values were tried out to find values that lead to a good optimization result. The final choice of settings are shown in Table 4.3.

4.3 Optimization Results

For the final optimization we fly 15000 particles with an energy of 1300 eV for each individual simulation. One simulation takes about 30 s with an Intel(R) Core(TM) i7-7500U CPU @ 2.70GHz. With a population size of 50 and 100 generations this leads to an optimization time of almost two days. Over the course of the optimization, the

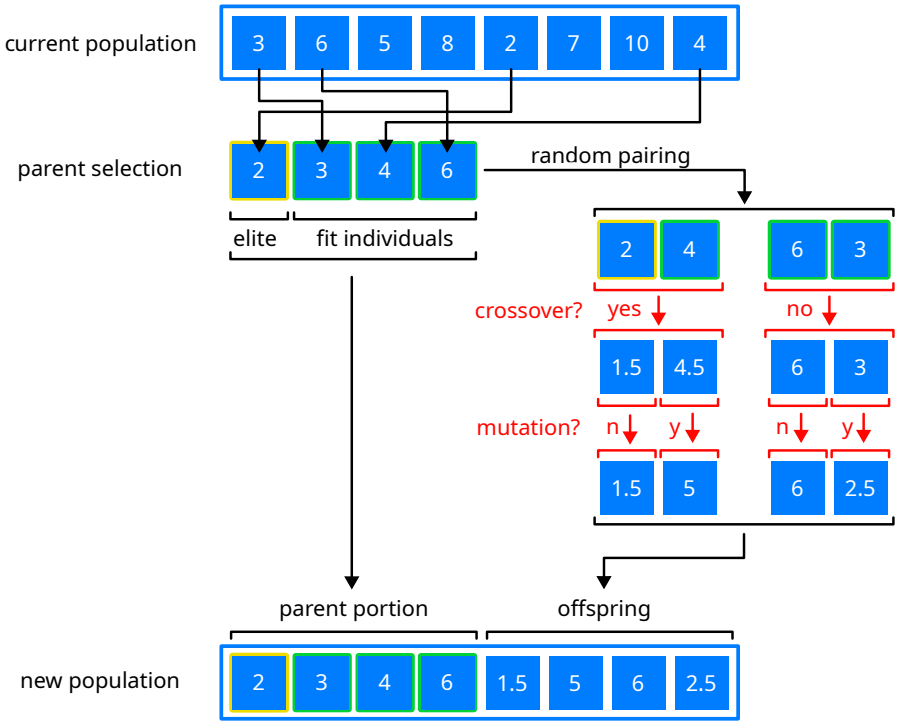

Figure 4.2: Visualization of genetic algorithm. Squares represent individual solutions and the number their fitness (the smaller the better). According to the parent portion, a number of parents needs to be selected from the current population. A number of elite individuals is always selected, according to the elite ratio. The remaining parents are selected with a probability proportional to their fitness (the better the fitness, the more likely the solution will be picked). When the parent pool is complete, random pairs are drawn from it. The pairs have a probability to undergo crossover, resulting in offspring with new properties or copying of the old properties. After that, each offspring has a probability to undergo a random mutation. The parents and the offspring are then combined to the new population. This process represents the evolution of one generation.

fitness was gradually decreased. The fitness over the generation number is depicted in Figure 4.3. The decrease is monotonous, since the algorithm works with elitism. Should the algorithm fail to find a better individual solution in generation n, then the best solution of generation n equals the best solution of generation $n-1$. The best parameters found by the optimization are shown in Table 4.4. The optimal voltage for the found geometry is $-267\,\mathrm{V}$ for a $1300\,\mathrm{eV}$ primary beam. This leads to the important ratio r_{NIOS} between the voltage and the primary beam energy

$$r_{\mathrm{NIOS}} = \frac{-267\,\mathrm{V}}{1300\,\mathrm{eV}} \approx -0.2\,\frac{\mathrm{V}}{\mathrm{eV}}. \tag{4.6}$$

The ratio dictates the necessary NIOS voltage for a specific beam energy.

The final geometry is shown in Figure 4.4. The new design features three electrodes

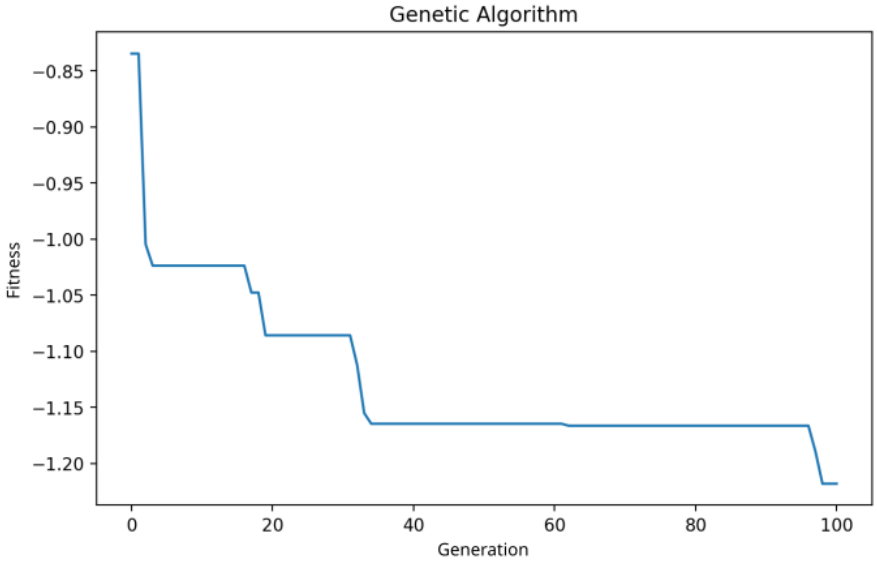

Figure 4.3: Fitness over generation. The fitness is minimized over the course of 100 generations. One generation consists of 50 individuals.

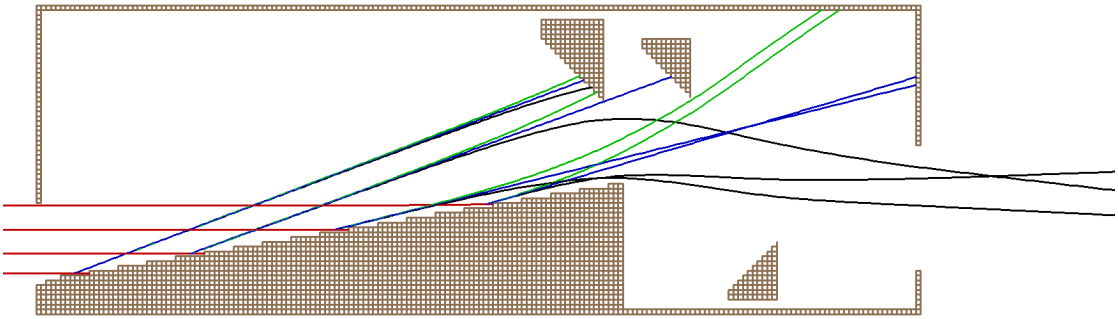

Figure 4.4: Optimized NIOS model with example trajectories. Primary ions are drawn in red, scattered positive ions in green, neutrals in blue and negative ions in black.

instead of four. This decision follows multiple trial optimizations with different designs. Removing the horizontal electrode and one of the vertical ones and adding an electrode in the lower right corner provided the best results. The figure also illustrates the trajectories of four primary ions and their scattering products. The positively charged scattered ions (green) are successfully filtered out, as well as the neutrals (blue). The negative ions are guided outside, unless they are created at the very front of the scattering surface (left side).

The new design was handed over to the engineers at IRF. With the help of CAD software a technical drawing (see Figure 4.5) was created which is used to manufacture the parts in the workshop at IRF. The finished and assembled new NIOS can be seen

Table 4.4: Table showing parameters defining optimized NIOS. The table contains the fixed geometry parameters and the free ones. It also contains the optimal electrode voltage for a 1300 eV beam.

Parameter	Value [mm]	Type
wall	2	fixed
boxx	180	fixed
boxy	60	fixed
entrance_ymin	5	fixed
entrance_ymax	20	fixed
surface_endx	120	fixed
surface_endy	25	fixed
elec1_l	12	fixed
elec1_d	10	fixed
elec2_l	17	fixed
elec2_d	13	fixed
elec3_l	12	fixed
elec3_d	10	fixed
exit_ymin	8	free
exit_ymax	32	free
elec1_x	124	free
elec1_gap	5	free
elec2_x	103	free
elec2_gap	1	free
elec3_x	152	free
elec3_gap	1	free
voltage	−267 V	free

in Figure 4.6. In this version the scattering surface is not covered by vapor deposited aluminium tape. Instead it was milled with a high precision diamond milling head, which provides a to a high degree mirror like smooth surface.

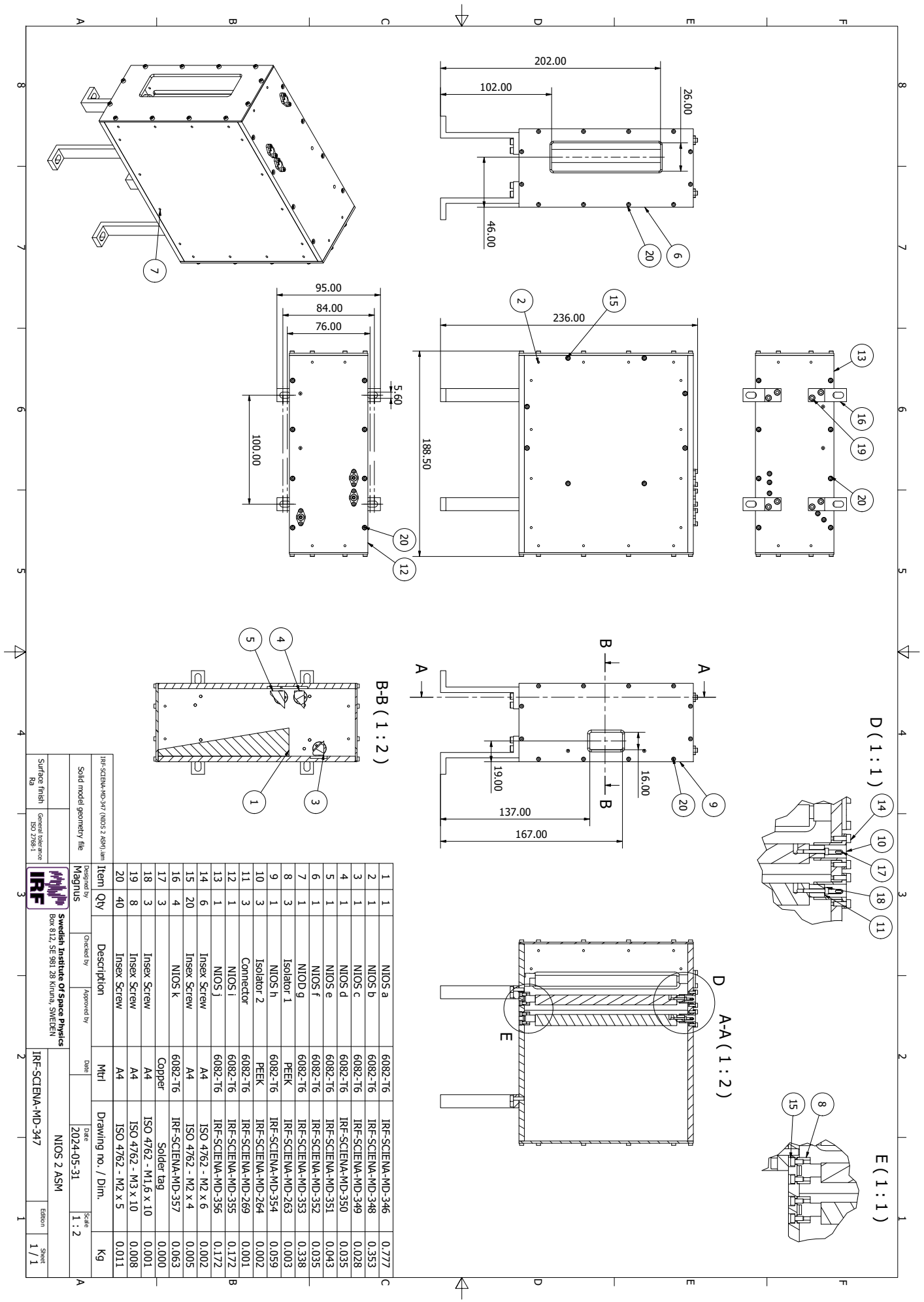

Item	Qty	Description	Mtrl	Drawing no. / Dim.	Kg
1	1	NIOS a	6082-T6	IRF-SCIENA-MD-346	0.777
2	1	NIOS b	6082-T6	IRF-SCIENA-MD-348	0.353
3	1	NIOS c	6082-T6	IRF-SCIENA-MD-349	0.028
4	1	NIOS d	6082-T6	IRF-SCIENA-MD-350	0.035
5	1	NIOS e	6082-T6	IRF-SCIENA-MD-351	0.043
6	1	NIOS f	6082-T6	IRF-SCIENA-MD-352	0.035
7	1	NIOD g	6082-T6	IRF-SCIENA-MD-353	0.338
8	3	Isolator 1	PEEK	IRF-SCIENA-MD-263	0.003
9	1	NIOS h	6082-T6	IRF-SCIENA-MD-354	0.059
10	3	Isolator 2	PEEK	IRF-SCIENA-MD-264	0.002
11	3	Connector	6082-T6	IRF-SCIENA-MD-269	0.001
12	1	NIOS i	6082-T6	IRF-SCIENA-MD-355	0.172
13	1	NIOS j	6082-T6	IRF-SCIENA-MD-356	0.172
14	6	Insex Screw	A4	ISO 4762 - M2 x 6	0.002
15	20	Insex Screw	A4	ISO 4762 - M2 x 4	0.005
16	4	NIOS k	6082-T6	IRF-SCIENA-MD-357	0.063
17	3		Copper	Solder tag	0.000
18	3	Insex Screw	A4	ISO 4762 - M1,6 x 10	0.001
19	8	Insex Screw	A4	ISO 4762 - M3 x 10	0.008
20	40	Insex Screw	A4	ISO 4762 - M2 x 5	0.011

IRF-SCIENA-MD-347 (NIOS 2 ASM).iam
Solid model geometry file
Designed by: Magnus
Checked by:
Approved by:
Date: 2024-05-31
Surface finish Ra
General tolerance ISO 2768-1
Swedish Institute Of Space Physics
Box 812, SE 981 28 Kiruna, SWEDEN
IRF-SCIENA-MD-347
NIOS 2 ASM
Scale: 1 : 2
Sheet: 1 / 1
Edition

Figure 4.5: Technical drawing of improved NIOS, provided by IRF.

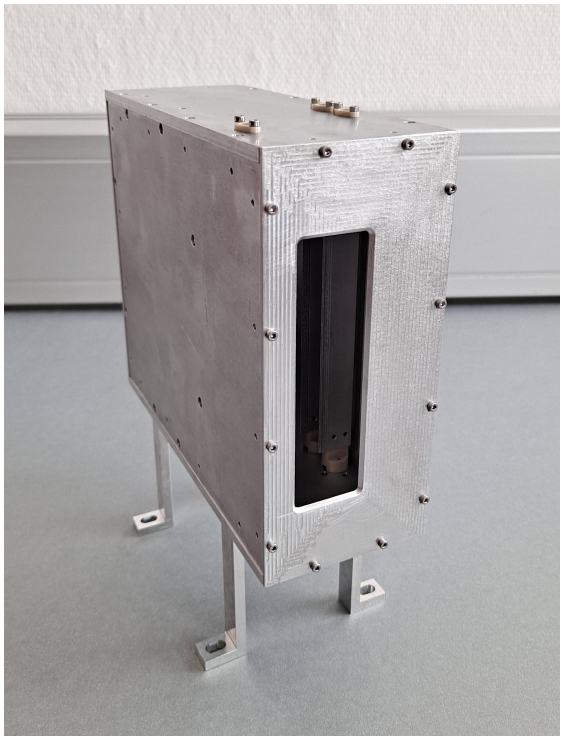

Figure 4.6: Physical model of improved NIOS. The visible aperture is the exit aperture. One of the electrodes can be seen through the aperture. On the top surface there are insulator elements, which insulate the electrodes from the body.

4.4 Optimization Discussion

The third and final goal of this work was to improve the design of NIOS. This was achieved by using a genetic algorithm to minimize a fitness function. Out of the vast field of optimization algorithms a genetic algorithm seemed to be one of the appropriate choices. The genetic algorithm capable of probing the multi-dimensional parameter space, without getting stuck easily in a local optimum. The behavior of the fitness function upon parameter changes is not obvious, since the parameters are not direct terms in the function. The parameters only indirectly influence the terms, by changing the geometry of NIOS, resulting in different ion counts. Therefore we chose a robust algorithm over a potentially faster one. The fitness function has a simple linear structure, except for the parallelity factor. Other design approaches such as working with logarithmic terms can potentially improve the result further.

In Figure 4.7 we see both new and old design in comparison. The electrodes have moved towards the exit. This way, the primary ions are not bent upwards, away from the scattering surface. The new design does not allow for primary ions to pass through NIOS without surface interaction (compare with red particles of old design). All primary ions that enter NIOS actually hit the scattering surface and unwanted scattered particles

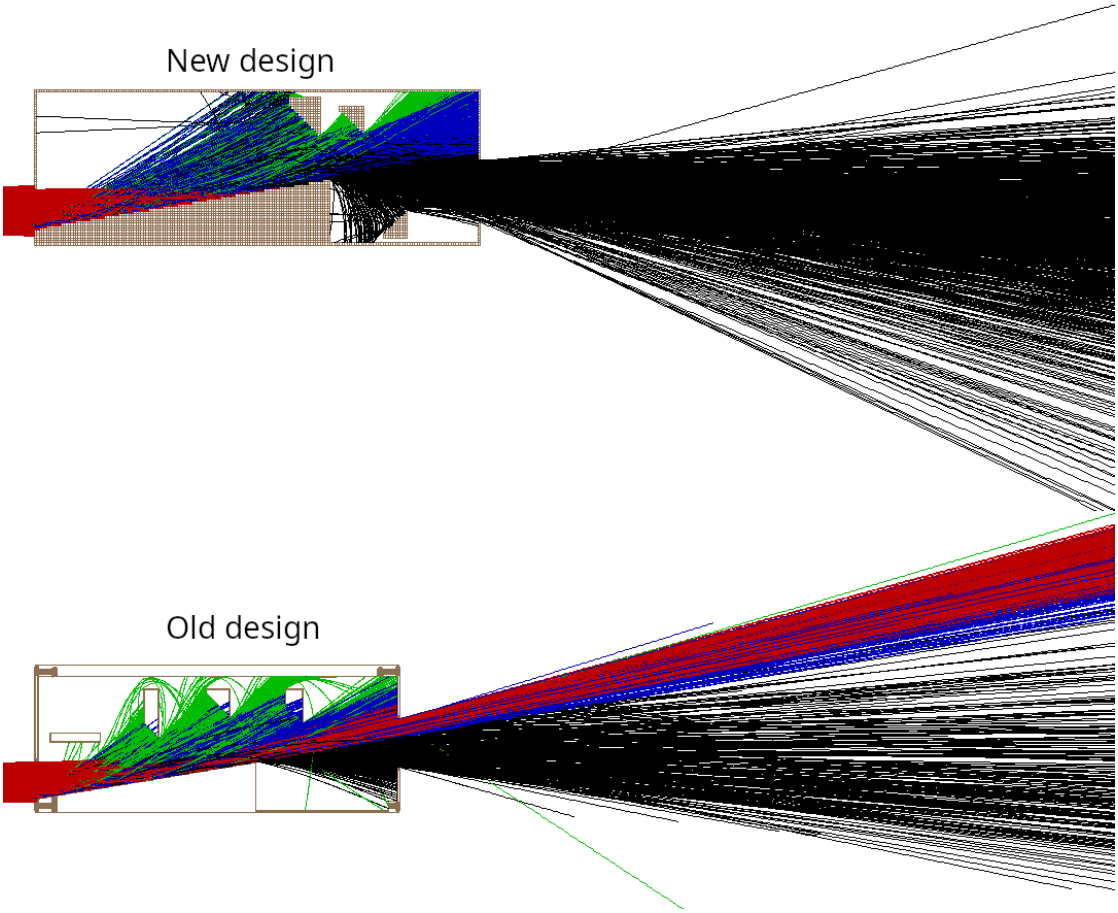

Figure 4.7: Comparison of particle trajectories for old and new NIOS design. Primary ions are red, neutral scattered atoms are blue, scattered positive ions are green and scattered negative ions are black.

are hindered from leaving NIOS. An additional electrode in the lower half pushes the negative ions back up, such that the bulk velocity is more parallel to the primary beam line. The first three problems mentioned at the beginning of this chapter are therefore addressed by the new design (primary ions flying through NIOS, unscattered primaries, and unwanted scattered particles leaving NIOS).

In order to have a quantitative measure for the improvement we take a look at Figure 4.8. It shows two simulated z-scans, from the old and from the new design. The counts

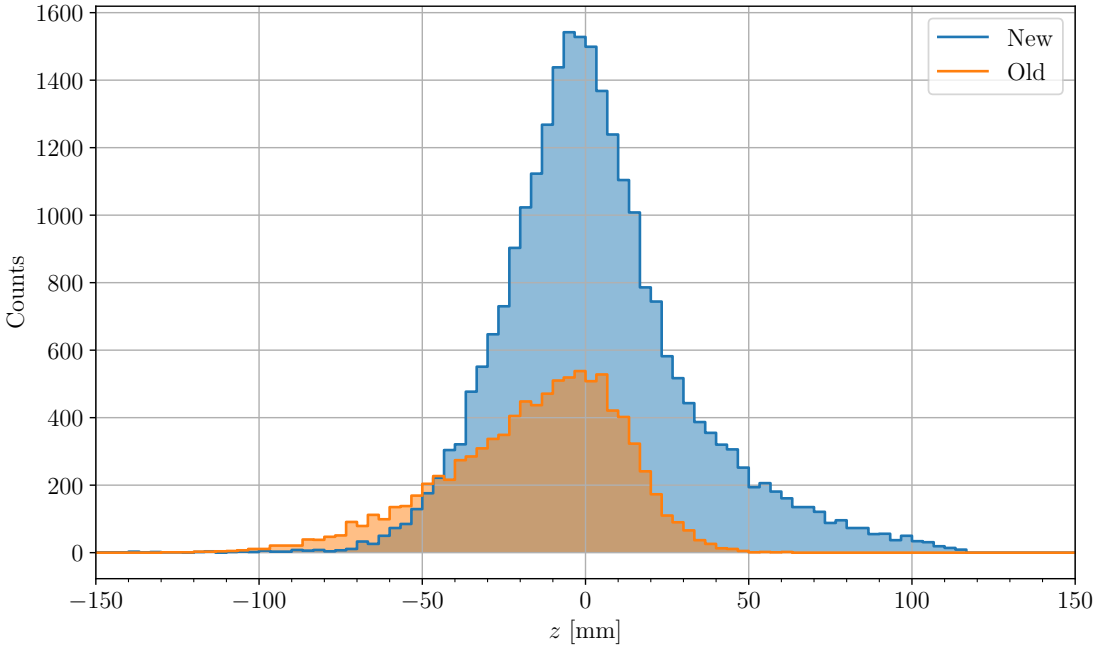

Figure 4.8: Comparison between z-scan of old and new NIOS design. y-axis shows negative ion counts.

represent negative ions registered at the detection surface. The peak count number and the total summed counts have increased by a factor of 2.7. We define the negative ion yield as the ratio of counted negative ions at the detection surface and the amount of primary ions. The ratio takes the conversion efficiency of 5 % for ions into account. The new design has an ion yield of 1.27 % compared to 0.47 % for the old design. This addresses the last problem, mentioned at the beginning of this chapter (negative ion yield).

The optimization was done for one specific energy, 1300 eV, resulting in a specific set of optimized parameters for geometry and NIOS voltage. The NIOS voltage, together with the primary beam energy, led to the ratio $r_{\mathrm{NIOS}} = -0.2\,\mathrm{V\,eV^{-1}}$. This ratio is optimized for a primary energy of 1300 eV as well. The ratio can be used for all energies, but the performance might decrease the larger the difference is between the primary energy and 1300 eV. One easy way to address this problem is to run another optimization where we use the newly found geometry described above and only optimize the NIOS voltage for different primary energies. This would lead to an energy dependent ratio $r_{\mathrm{NIOS}}(E)$.

These improvements and findings conclude the optimization part of this work. The improved NIOS has been manufactured at IRF and is going to be used for the calibration of future particle instruments.

5 Conclusion

Among the many processes produced by solar wind - Moon interactions are scattering and sputtering. Both processes are believed to create negative ions. These ions have never been observed so far. The NILS instrument, built by IRF, onboard the Chang'E-6 spacecraft is dedicated to to find negative ions at the lunar surface. The negative ions for the calibration of NILS were provided by the charge conversion particle source NIOS.

This thesis aimed to fullfil three tasks:

1. Characterize NIOS in the calibration facility of IRF in order to calibrate the NILS instrument.
2. Simulate the interaction between NIOS and the primary ion beam with the software package SIMION.
3. Optimize the geometry and develop an improved NIOS with the help of the simulation.

The data acquired during the characterization was successfully used for the calibration of NILS. The characterization helped to identify problems with NIOS that were subject to improvement during the optimization. For example, a portion of the primary beam went through NIOS without ever interaction with a surface.

With SIMION and the manually implemented physical features *scattering, charge conversion, molecule dissociation,* and *Earth's magnetic field*, we were able to simulate the interaction between NIOS and the positive ion beam. We discovered that the implementation of secondary electron emission was not able to explain the electrons measured by NILS. The most likely cause for that is the lack of multiple scattering.

The characterization data proved to be valuable to validate and improve the simulation of NIOS. The energy-distribution function was adjusted such that the simulation fits best to the measured NIOS profile for a primary beam with an energy of 1300 eV. Potential for improvement lies in the definition of the energy-distribution function. Its implementation is energy-independent, which is a simplification. In reality it depends on the incident beam energy.

The simulation allowed us to optimize the geometry and voltage of NIOS for an energy of 1300 eV. The optimization yielded an optimal NIOS voltage of $-267\,\mathrm{V}$ for the particular beam energy, resulting in a ratio between NIOS voltage and primary beam of $r_{\mathrm{NIOS}} = -0.2\,\mathrm{V/eV}$. Multiplying this ratio with the primary beam energy gives the suggested NIOS voltage to use. The negative ion yield has increased by a factor of 2.7 from 0.47 % for the old model to 1.27 % for the new model. The new model has been manufactured and is going to be used for future instrument calibration campaigns.

6 Acknowledgments

To me, the fact that I am writing these acknowledgments right now is almost unbelievable. If I could time-travel back and tell my younger self in middle school "You are going to study physics and write your thesis at the Swedish Institute of Space Physics in Lapland.", I would not have believed a single word. When I take a look back at my journey that led me to this place I am astonished. The fact that I got accepted into and financially supported by the Studienstiftung des deutschen Volkes was such an immense help. I want to express my sincere gratitude to this amazing institution. Without it, I could not have spent an exchange year in Umeå, I never would have taken the course "Arctic Science" and I never would have visited IRF and Kiruna.

In 2022 I walked the Camino de Santiago and one of my personal goals was it to make a decision whether I wanted to commit to a thesis in the Arctic or not. I discussed this with a handful of then strangers and every single one advised me to do it, and here I am. Of course, I also would not know what I missed out on, but what I do know is that through these decisions I have discovered places that I have fallen in love with. I have met amazing people, generous, helpful, and in general nice to have around.

I want to particularly name my supervisor at IRF, Martin Wieser. Your supervision has been exceptionally good in both quality and frequency and you have taught me much more than what is written in this thesis. I highly appreciate your support, which went far beyond what is necessary and the support did not stop at the front door of IRF either. Thank you for integrating me in the community from the first day on.

I also want to name my supervisor at FAU, Jörn Wilms. Our regular meetings and your input helped me a lot to stay on track and go forward. Thank you very much for your trust in me while I was so far away. Without you this endeavor would not have been possible.

What ever lies ahead, so far it has been an amazing ride. Thank you to everyone who was with me during this time – from family to friends, from fellow students to teachers. I am unbelievably grateful that I have had the chance to experience all of this and I am looking forward to the future.

Bibliography

Angelopoulos, V. The ARTEMIS Mission. *Space Science Reviews*, 165(1):3–25, 2011. doi: 10.1007/s11214-010-9687-2.

Barabash, S., Bhardwaj, A., Wieser, M., Sridharan, R., Kurian, T., Varier, S., Vijayakumar, E., Abhirami, V., et al. Investigation of the solar wind-Moon interaction onboard Chandrayaan-1 mission with the SARA experiment. *Current Science*, 96:526–532, 2009. URL https://www.jstor.org/stable/24105464.

Bhattacharya, R., Eckstein, W., and Verbeek, H. Positive charge fractions of H, D, and He backscattered from solid surfaces. *Surface Science*, 93(2-3):563–581, 1980. doi: 10.1016/0039-6028(80)90283-6.

Borovsky, J. E. What magnetospheric and ionospheric researchers should know about the solar wind. *Journal of Atmospheric and Solar-Terrestrial Physics*, 204:105271, 2020. doi: 10.1016/j.jastp.2020.105271.

Carter, T. L. Ion Sources for the Production of Low Energy Beams. MA Thesis, United States Naval Postgraduate School, 1968. URL https://hdl.handle.net/10945/12515.

Crider, D. H. and Vondrak, R. R. Hydrogen migration to the lunar poles by solar wind bombardment of the moon. *Advances in Space Research*, 30(8):1869–1874, 2002. doi: 10.1016/S0273-1177(02)00493-3.

Dahl, D. A. SIMION for the personal computer in reflection. *International Journal of Mass Spectrometry*, 200(1):3–25, 2000. doi: 10.1016/S1387-3806(00)00305-5.

Eiben, A. and Smith, J. *Introduction to Evolutionary Computing*. Natural Computing Series. Springer-Verlag Berlin Heidelberg, 2015. doi: 10.1007/978-3-662-44874-8.

Goldberg, D. E. *Genetic Algorithms in Search, Optimization and Machine Learning*. Addison-Wesley Longman Publishing Co., Inc., 1st edition, 1989.

Grava, C. and Retherford, K. D. Lunar Atmosphere. In Cudnik, B., editor, *Encyclopedia of Lunar Science*. Springer Nature Switzerland AG, 2023.

Heiland, W. The Interaction of Molecular Ions with Surfaces. In Rabalais, J. W., editor, *Low Energy Ion-Surface Interactions*, Wiley Series on Ion Chemistry and Physics. John Wiley & Sons, 1994.

Hoffman, J. H. and Hodges, R. R. Molecular gas species in the lunar atmosphere. *The moon*, 14(1):159–167, 1975. doi: 10.1007/BF00562981.

Holmström, M., Wieser, M., Barabash, S., Futaana, Y., and Bhardwaj, A. Dynamics of solar wind protons reflected by the Moon. *Journal of Geophysical Research: Space Physics*, 115(A6):2009JA014843, 2010. doi: 10.1029/2009JA014843.

L'Hoir, A. Study of the asymmetrical response of silicon surface barrier detectors to MeV light ions. Application to the precise analysis of light ions energy spectra I. Helium ions. *Nuclear Instruments and Methods in Physics Research*, 223(2):336–345, June 1984. doi: 10.1016/0167-5087(84)90671-9.

Lue, C., Futaana, Y., Barabash, S., Wieser, M., Holmström, M., Bhardwaj, A., Dhanya, M. B., and Wurz, P. Strong influence of lunar crustal fields on the solar wind flow. *Geophysical Research Letters*, 38(3), 2011. doi: 10.1029/2010GL046215.

Manura, D. J. and Dahl, D. A. *SIMION Version 8.0 User Manual*. Scientific Instrument Services, Inc., document revision 4 edition, 2008.

McComas, D. J., Allegrini, F., Bochsler, P., Bzowski, M., Collier, M., Fahr, H., Fichtner, H., Frisch, P., et al. IBEX—Interstellar Boundary Explorer. *Space Science Reviews*, 146(1):11–33, 2009a. doi: 10.1007/s11214-009-9499-4.

McComas, D. J., Allegrini, F., Bochsler, P., Frisch, P., Funsten, H. O., Gruntman, M., Janzen, P. H., Kucharek, H., Möbius, E., Reisenfeld, D. B., and Schwadron, N. A. Lunar backscatter and neutralization of the solar wind: First observations of neutral atoms from the Moon. *Geophysical Research Letters*, 36(12), 2009b. doi: 10.1029/2009GL038794.

National Research Council. *The Scientific Context for Exploration of the Moon*. National Academies Press, Washington, D.C., 2007. doi: 10.17226/11954.

Niehus, H., Heiland, W., and Taglauer, E. Low-energy ion scattering at surfaces. *Surface Science Reports*, 17(4):213–303, 1993. doi: 10.1016/0167-5729(93)90024-J.

Ouyang, Z., Li, C., Zou, Y., Zhang, H., Lü, C., Liu, J., Liu, J., Zuo, W., et al. Primary scientific results of Chang'E-1 lunar mission. *Science China Earth Sciences*, 53(11): 1565–1581, 2010. doi: 10.1007/s11430-010-4056-2.

Pieters, C. M., Goswami, J. N., Clark, R. N., Annadurai, M., Boardman, J., Buratti, B., Combe, J.-P., et al. Character and Spatial Distribution of OH/H2O on the Surface of the Moon Seen by M3 on Chandrayaan-1. *Science*, 326(5952):568–572, 2009. doi: 10.1126/science.1178658.

Saito, Y., Yokota, S., Asamura, K., Tanaka, T., Akiba, R., Fujimoto, M., Hasegawa, H., Hayakawa, H., et al. Low-energy charged particle measurement by MAP-PACE onboard SELENE. *Earth, Planets and Space*, 60(4):375–385, 2008. doi: 10.1186/BF03352802.

Scott, K. and Pain, C. *Regolith Science*. Springer Dordrecht, 1 edition, 2009.

Seiler, H. Secondary electron emission in the scanning electron microscope. *Journal of Applied Physics*, 54(11):R1–R18, 1983. doi: 10.1063/1.332840.

Smith, M., Craig, D., Herrmann, N., Mahoney, E., Krezel, J., McIntyre, N., and Goodliff, K. The Artemis Program: An Overview of NASA's Activities to Return Humans to the Moon. In *2020 IEEE Aerospace Conference*, pages 1–10, 2020. doi: 10.1109/AERO47225.2020.9172323.

Verbeek, H., Eckstein, W., and Bhattacharya, R. S. Negative hydrogen ion formation by backscattering from solid surfaces. *Surface Science*, 95(2):380–390, 1980. doi: 10.1016/0039-6028(80)90184-3.

Wekhof, A. Negative ions in the ionospheres of planetary bodies without atmospheres. *The moon and the planets*, 24(1):45–52, 1981. doi: 10.1007/BF00897567.

Wieser, M. Experimental Work for the Direct Measurement of Interstellar Neutral Gas. Master's thesis, University of Bern, 2001. URL https://www.iapetus.ch/doc/diploma/.

Wieser, M. *Detection of Energetic Neutral Atoms and its Application to Heliospheric Science*. PhD Thesis, University of Bern, 2005. URL https://www2.irf.se/~wieser/wieser-2005-dissertation.pdf.

Wieser, M. Negative Ions at the Lunar Surface (NILS), an instrument proposal in response to CNSA's Announcement of Opportunity for Scientific Payloads onboard Chang'E-6 Mission. Technical report, Swedish Institute of Space Physics, 2019.

Wieser, M., Wurz, P., Brüning, K., and Heiland, W. Scattering of atoms and molecules off a magnesium oxide surface. *Nuclear Instruments and Methods in Physics Research Section B: Beam Interactions with Materials and Atoms*, 192(4):370–380, 2002. doi: 10.1016/S0168-583X(02)00486-X.

Wieser, M., Barabash, S., Wang, X.-D., Grigoriev, A., Zhang, A., Wang, C., and Wang, W. The Advanced Small Analyzer for Neutrals (ASAN) on the Chang'E-4 Rover Yutu-2. *Space Science Reviews*, 216(4):73, 2020. doi: 10.1007/s11214-020-00691-w.

Wieser, M., Williamson, H., Wieser, G. S., Barabash, S., Zhang, A., Wang, C., and Wang, W. Energy spectra of energetic neutral hydrogen backscattered and sputtered from the lunar regolith by the solar wind. *Astronomy & Astrophysics*, 684:A146, 2024. doi: 10.1051/0004-6361/202348876.

Willis, R. F., Anderegg, M., Feuerbacher, B., and Fitton, B. Photoemission and Secondary Electron Emission from Lunar Surface Material. 37:389, 1973. doi: 10.1007/978-94-010-2647-5_25.

Wittmann, P. *The Jovian Plasma Dynamics and Composition Analyzer (JDC) for ESA's JUICE Mission*. PhD Thesis, Umeå University; Institutet för Rymdfysik, 2022. URL https://urn.kb.se/resolve?urn=urn%3Anbn%3Ase%3Aumu%3Adiva-193773.

Wuest, M., Evans, D. S., and von Steiger, R., editors. *Calibration of Particle Instruments in Space Physics*. SR-007. International Space Science Institute, 2007.

Xin, L. What China's mission to collect rocks from the Moon's far side could reveal. *Nature*, 629(8011):265–266, 2024. doi: 10.1038/d41586-024-01056-x.

Yamauchi, M., Luspa, M., Mikhaylova, D., and Brandström, U. Kiruna Magnetometer 1-min Data in ASCII Flat Table Format, Swedish Institute of Space Physics, 2024. URL https://doi.org/10.48322/7xsf-ze79.

Selbstständigkeitserklärung

Hiermit bestätige ich, dass ich diese Arbeit selbstständig und nur unter Verwendung der angegebenen Hilfsmittel und Quellen angefertigt habe.

Ort, Datum	Maximilian Wecker